Pool boiling investigation on copper foam with heterogeneous wetting vapor channels

Xiao Yuan[1, 2], Yanping Du[3, *], Jing Su[4], Yu Lin[1], Jinwen Shi[5,*], Chao Wang[6,*]

[1]Midea Group Kitchen & Water Heater Appliance, Midea Group Innovation Center, 528311, Foshan, China.

[2]China-UK Low Carbon College, Shanghai Jiao Tong University, Shanghai, 201306, China.

[3]School of Engineering, Lancaster University, Lancaster LA14YW, UK.

[4]Jiangsu Engineering Technology Research Centre of Functional Textiles, Jiangnan University, 214122, Wuxi, China.

[5]International Research Center for Renewable Energy, State Key Laboratory of Multiphase Flow in Power Engineering, Xi'an Jiaotong University, Xi'an 710049, China

[6]School of Materials and Energy, Guangdong University of Technology, Guangzhou 510006, China

* Correspondence: y.du17@lancaster.ac.uk;

jinwen_shi@mail.xjtu.edu.cn

chaowang@gdut.edu.cn

Abstract: This study presents a pool boiling experimental investigation of copper foam microchannels with engineered heterogeneous wettability conducted under atmospheric conditions. Copper foam microchannels with spatially varied wetting properties were fabricated using immersion and welding methods. Two specific configurations were developed: one featuring super hydrophilic channel walls with a super hydrophobic bottom surface (SHPiW–SHPoB), and the other comprising superhydrophobic walls combined with a super hydrophilic bottom surface (SHPoW–SHPiB). By experiments, the effects of wettability heterogeneity on boiling heat transfer performance were systematically evaluated. It is found that the SHPiW–SHPoB configuration demonstrates a superior critical heat flux (CHF) of 108.2 W/cm², compared to 96.7 W/cm² for the SHPoW–SHPiB. Further experimental results show that the SHPiW–SHPoB configuration offers significantly improved pool boiling characteristics, indicating the potential of the wettability patterning for advanced thermal management of energy systems. The experiments suggest that the enhanced boiling performance of the SHPiW–SHPoB is attributed to the efficient separation of vapor and liquid flow paths enabled by the heterogeneous wetting design, which promotes bubble nucleation at low heat fluxes and suppresses bubble coalescence at

high heat fluxes.

Key words: Immersion method; Copper foam microchannel; Pool boiling; Heterogeneous wettability.

Nomenclature		*Abbreviations*	
		CHF	critical heat flux
q	heat flux, [W/cm^2]	HTC	heat transfer coefficient
h	heat transfer coefficient, [W/cm^2·K]	ONB	onset of nucleate boiling
ΔT	wall superheat, [K]	UTP	untreated plain copper foam
N_a	nucleation site density, [cm^{-2}]	SHPiP	super-hydrophilic plain copper foam
D_b	bubble departure diameter, [mm]	SHPoP	super-hydrophobic plain copper foam
f	bubble departure frequency, [sec^{-1}]	UTM	untreated copper foam microchannel
Greek symbols		SHPiM	super-hydrophilic copper foam microchannel
δ_t	thermal boundary layer thickness	SHPoM	super-hydrophobic copper foam microchannel
θ	contact angle, [°]	SHPiW-SHPoB	copper foam microchannel with super-hydrophilic wall and super-hydrophobic bottom
σ	surface tension	SHPoW-SHPiB	copper foam microchannel with super-hydrophobic wall and super-hydrophilic bottom
ρ_v	vapor density		
ρ_l	liquid density		
h_{fg}	latent heat of vaporization		

1. Introduction

The ongoing trend towards integration and miniaturization in microelectronic devices demands high-density heat dissipation technologies to ensure safe and reliable operations [1,2]. Effective thermal management of such high energy density systems requires advanced thermal management solutions capable of removing substantial amounts of heat within confined spaces. Among various methods, pool boiling heat transfer has emerged as a promising approach due to the large latent heat of vaporization during the boiling phenomenon. Pool boiling performance is typically characterized by the onset of nucleate boiling (ONB), the heat transfer coefficient (HTC) and the critical heat flux (CHF). ONB shows the temperature at which boiling initiates, HTC reflects the efficiency of heat transfer during boiling, while CHF marks the upper limit of the nucleate boiling regime before the deterioration of heat transfer. Therefore, all the above need to be considered for enhancing the boiling performance. Traditional strategies include increasing the heat transfer surface area, augmenting nucleation site density, and improving capillary-driven liquid replenishment have been extensively explored. However, the coupling of the above key parameters has not well resolved.

With in-depth research on micro-nano heat transfer, numerous micro/nano structures which can improve pool boiling heat transfer, including microchannels [3-5], micro pillars [6-8], micro fins [9-11], micro porous media [12-14], nanowires [15-17], nanotubes [18-20], nanopores [21, 22] and micro-nano hierarchical structures [23-25] have been extensively applied. Essentially, Pool boiling heat transfer can be significantly enhanced by manipulating bubble dynamics through engineered micro/nanostructures. Among various surface modifications, metal foam has gained considerable attention as a porous material capable of improving boiling performance. Xu et al. [26] used acetone as the heat transfer fluid and concluded that the pore density of copper foam markedly affected the boiling heat transfer performance. Manetti et al. [27] further reported that foam thickness played a critical role with thinner copper foams enhancing both the critical heat flux (CHF) and heat transfer coefficient (HTC) due to reduced vapor escape resistance and improved capillary wicking. Hu et al. [28, 29] showed that hydrophilic surface modification could substantially increase the CHF of copper foams. In addition, Shi et al. [30] found that introducing super hydrophilic micro/nanostructures to copper foam surfaces significantly enhanced pool boiling performance due to the increasing of the density of nucleation sites and the facilitating of more effective liquid replenishment.

The aforementioned studies indicate that enhancing nucleation site density, increasing surface area, and strengthening capillary-driven liquid replenishment are key strategies for improving pool boiling heat transfer in various conditions. Metal foams with high pore density offer more nucleation sites; however, an excessive number of active sites can lead to bubble crowding and increased vapor resistance, leading to boiling deterioration at high heat fluxes. To address this issue, a novel approach involving metal foams integrated with vapor channels has been proposed to reduce vapor escape resistance by decoupling the liquid and vapor flow paths. For example, Sharifzadeh et al. [31] demonstrated that optimized copper foam with a 5 mm diameter vapor channel achieved a maximum heat transfer coefficient (HTC) of 13.56 $W/cm^2 \cdot K$. Similarly, Li et al. [32] reported that the HTC at high heat fluxes could be significantly improved by optimizing both the diameter and number of vapor channels within the copper foam. In addition, the use of gradient-structured metal foams has shown considerable promise in facilitating bubble escape and enhancing boiling performance. For instance, Zhou et al. [33] found that foams with pore-density gradients significantly influenced the heat transfer enhancement. Huang et al. [34] further revealed that more heat could be dissipated when bubbles detached upward, while the frequency of bubble release increased when bubbles escaped laterally. These studies necessities the optimized design of pore density of metal foams.

Overall, enhancements in pool boiling performance can be achieved through the use of metal foams with optimized thickness, pore density, surface wettability, vapor channels, or pore-density gradients. However, the combined effects of foam wettability and integrated vapor channels have received limited attention in existing studies. In this work, the pool boiling performance of copper foams with heterogeneous wetting vapor channels are experimentally investigated. A visualized experimental setup was employed to observe and analyze the bubble behaviors at different conditions. By examining bubble dynamics on these structured copper foams, the synergistic enhancement by the interaction of the surface wettability and the vapor channel design is elucidated.

2. Experimental section

2.1 Materials

The structural parameters of copper foam are 20 mm × 20 mm, 40 PPI pore density, 94.3% porosity and 5 mm thickness. The copper foam's surface wettability can be modified using chemical method as follows.

Super-hydrophilic modification: Before super-hydrophilic modification, ultrasonic cleaning method was used to clean the original copper foams in an acetone solution, ethanol and DI water for 30 min step by step [35, 36]. Then, clean copper foams should be dried for 60 min in the vacuum oven. Noting that the chamber was purged with nitrogen to remove oxygen and prevent oxidation before vacuuming [36]. After drying process, clean copper foams can be modified in a 100 mL solution (1.25 M NaOH and 0.05 M $(NH_4)_2S_2O_8$) using chemical immersion method. When finishing the surface modification on the copper foam, DI water was used to wash the residue after chemical immersion. Also, these modified copper foams were dried in the vacuum oven [28, 29, 35, 36].

Super-hydrophobic modification: To create super-hydrophobic copper foam, above-mentioned super-hydrophilic copper foams can be submerged in a perfluorodecyltriethoxysilane (PFTS) solution with 1.0 wt% ethanol for 24h.

Copper foam microchannel: As show in **Figure 1a** and **b**, copper foam stripes measuring 3.5 mm width and 2.5 mm depth, as well as the copper foam bottom measuring 20 mm × 20 mm × 2.5 mm were used to conduct a wettability modification. As shown in **Figure 1c**, the spaced lead-free solder layer was paced on the copper foam bottom, and the copper foam stipes was firmly placed on the spaced solder layer using a heavy object. This was followed by that solder layer was melt until reaching its melting point under the effect of a heavy object when heating copper foam bottom. The spaced copper foam stripes were welded on the copper foam bottom when cooling to the room temperature. Then, modified copper foam stripes and bottoms were welded securely together to create a copper foam microchannel with various wetting properties (**Figure 1e** and **f**). According to the previous works [37, 38], for enhancing pool boiling performance of microchannel, the spacing between the microchannel must be equal to bubble departure diameter to prevent lateral coalescence. In these works, the bubble departure diameter obtained from Fritz equation resulted in a value of 2.21 mm which was in close correspondence to the critical capillary length of 2.5 mm [38]. 3 Based on this design, four types of heterogeneous wetting copper foam microchannels can be created using wettability modification and welding method (**Figure 2**). **Figure 2a** and **b** shows the uniform super-hydrophilic and super-hydrophobic copper foam microchannels, respectively.

SHPiW-SHPoB was manufactured by super-hydrophilic copper foam wall stipes and super-hydrophobic copper foam bottom (**Figure 2c**), and SHPoW-SHPiB was created by super-hydrophobic copper foam wall stripes and super-hydrophilic copper foam bottom (**Figure 2d**).

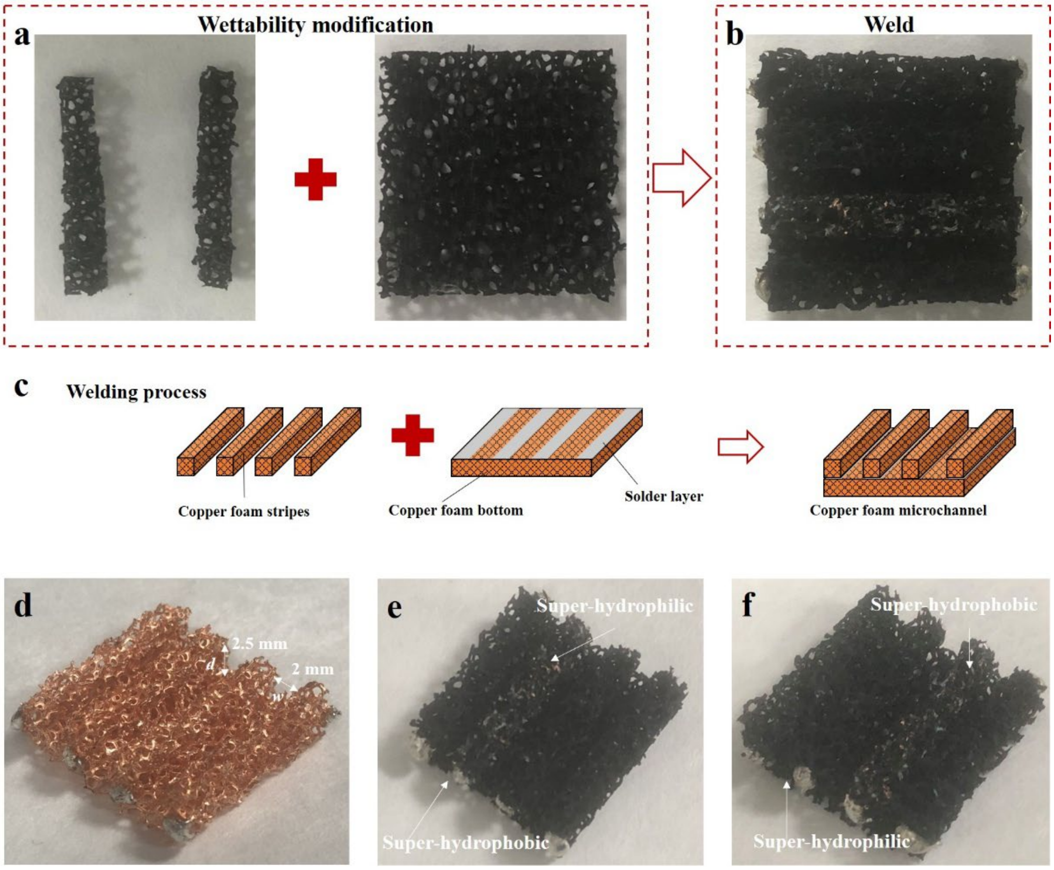

Figure 1. (a) Wettability modification of copper foam wall and copper foam bottom (b) Weld of copper foam microchannel (c) Welding process (d) Untreated copper foam microchannel (e) Copper foam microchannel with super-hydrophilic wall and super-hydrophobic bottom (f) Copper foam microchannel with superhydrophobic wall and super-hydrophilic bottom.

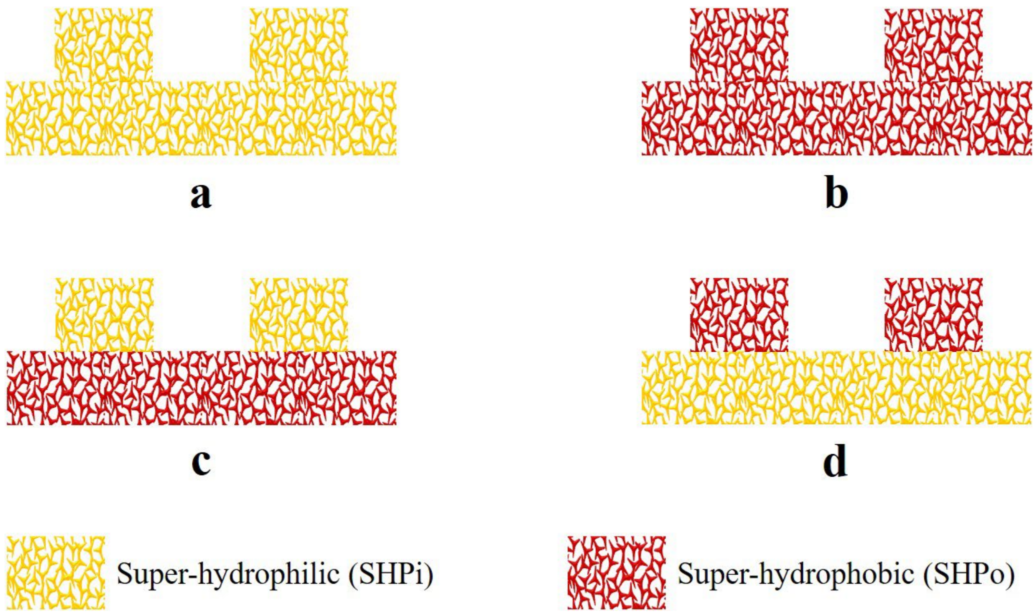

Figure 2. Four types of copper foam channel with wettability modification.

2.2 Surface features

Using a scanning electron microscope (SEM, Gemini 300, ZEISS), the microscopic morphology of the super-hydrophilic and super-hydrophobic micro/nanostructures on the copper foam was investigated. A contact angle meter (DSA 25S) was used to measure the contact angle at 25 °C and atmospheric pressure. The droplet volume for measuring the CA was 4 μL, and the droplet injection accuracy was 0.01 μL. Given the structural complexity of the copper foam, particularly its irregular pore distribution, the reported CA values represent the average of five measurements taken at different locations on each sample to ensure representative results.

2.3 Pool boiling experimental system

As shown in **Figure 3**, pool boiling experimental system mainly contains a boiling chamber, a heating system, a cooling system and a data acquisition system. When conducting boiling experiment, the 5 mm quartz glass boiling chamber was poured with DI water. Using the auxiliary heater around the PTFE block, DI water in the boiling chamber can be maintained at saturation under the atmospheric pressure. A spiral tube as a condenser, the boiling vapor can be condensed into a liquid. The main heating system involves the copper block, 3 cartridge heaters, DC power supply and AC autotransformer. And the head of copper block is 20 mm square and the bottom is cylindrical. The testing boiling surfaces were welded on the square top, and the 3 cartridge heaters, ranging in power from 0 to 1500 W were positioned in the cylinder bottom to continuously heat the boiling surface. Using the DC power supply and AC autotransformer, the heating power of copper block can be controlled. The PTFE block held the copper block together while maintaining the one-dimensional heat transfer.

As shown in Figure **3b**, along the square head of copper block, there were 9 thermocouples in the holes. Three thermocouples were distributed at 7 mm intervals. Through data acquisition system (Keysight, DAQ970A), temperature signals of thermocouples can be recoded every 30 seconds. Through recording temperature signals of thermocouples (T_{11}, T_{21}, T_{31}, T_{12}, T_{22}, T_{32}, T_{13}, T_{23} and T_{33}) on the square head of copper block, heat flux can be calculated (Figure **3b**). For measuring melting temperature of solder layer, thermocouples (T_{10}, T_{20} and T_{30}) on the top of the copper block were used (Figure **3c**). Using high-speed camera (Phantom VEO 410), bubble behavior during pool boiling process can be recorded at a resolution of 832 × 600 and 1000 frames per second (fps). As shown in **Figure 3d**, lead-free solder was used to weld copper foam microchannel onto the copper block. First, to create a thin coating of solder, the solder was placed on the top of copper block. Second, the solder layer on the copper block was melted through manipulating the voltage of the DC power source. Third, using the heavy object, the copper foam microchannel can be welded on copper block when cooling to the room temperature again.

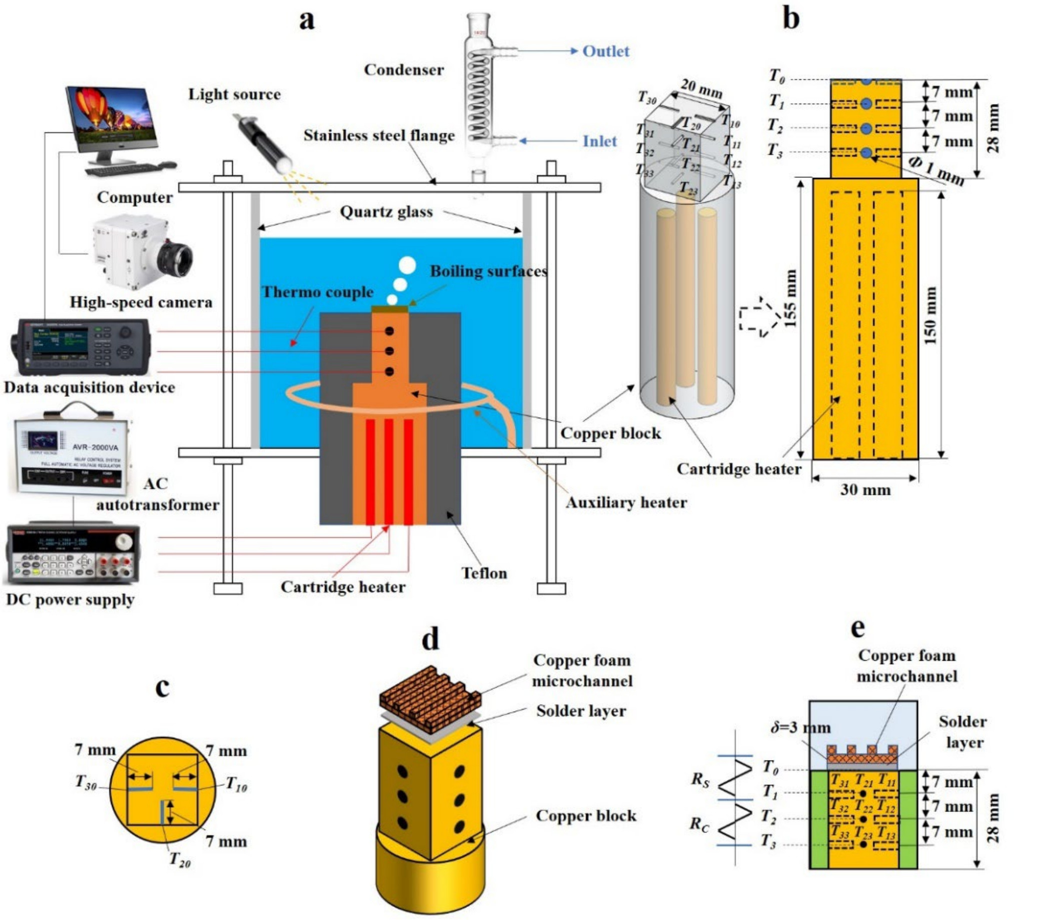

Figure 3. (a). Pool boiling experimental set-up (b). Copper block (c). Top view of copper block (d). Installation of copper foam microchannel (e). Resistance diagram for surface temperature calculation.

2.4 Experimental procedures and data reduction

To eliminate dissolved gases, deionized (DI) water was preheated to its saturation temperature (Tsat = 100 °C) and maintained for 60 minutes prior to the pool boiling experiments. The voltage was gradually raised to increase the heat flux. Initially, following a 15-minute stabilization period, the voltage was increased to 20 V. Subsequently, the voltage was raised in 5 V increments. Once the onset of nucleate boiling (ONB) was observed, the voltage increments were increased to 8 V steps. As the system approached the critical heat flux (CHF), the voltage was gradually reduced to 5 V intervals to capture the transition more precisely. CHF was identified by a sharp and sustained rise in surface temperature, indicating the transition to film boiling. At this point, the system was promptly shut down to prevent damage to the PTFE insulation block. To ensure repeatability and accuracy, each boiling test was performed three times per surface condition, and the average values were reported as the final results.

As shown in **Figure 3e**, average temperatures (T_0, T_1, T_2 and T_3) at the four planes can be calculated as follows:

$$T_0 = \frac{T_{10} + T_{20} + T_{30}}{3} \tag{1}$$

$$T_1 = \frac{T_{11} + T_{21} + T_{31}}{3} \tag{2}$$

$$T_2 = \frac{T_{12} + T_{22} + T_{32}}{3} \tag{3}$$

$$T_3 = \frac{T_{13} + T_{23} + T_{33}}{3} \tag{4}$$

Besides, one-dimensional heat transfer needs to be confirmed before calculating the heat flux. As shown in **Figure 4**, the temperature distribution at three locations (T_1, T_2 and T_3) along the square head of copper block was illustrated. The R-square values obtained from the linear temperature distribution across measurement points were consistently greater than 0.99, indicating strong linearity. This confirms that one-dimensional heat conduction occurs along the square head of the copper block, allowing the use of the one-dimensional form of Fourier's law to calculate the heat flux.

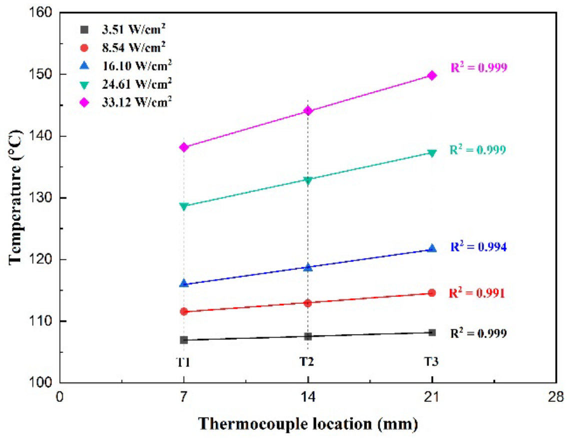

Figure 4. Temperature distribution at different heat fluxes.

According to the one-dimensional Fourier's law, the heat flux q can be calculated as below:

$$q = -\lambda_{Cu}\frac{dT}{dz} = \lambda_{Cu}\frac{T_3 - T_1}{\Delta z_{31}} \tag{5}$$

where λ_{Cu} is the thermal conductivity of the copper, dT/dz is the axial temperature gradient of the copper block calculated by the three temperatures measured by thermocouples, Δz is the distance between the adjacent thermocouple locations. As shown in **Figure 3e**, the contact thermal resistance (R_s) of solder layer exists between the copper block top and the copper foam microchannel bottom. Nevertheless, the contact thermal resistance with a thickness of 0.1 mm only occupies less than 1% of the entire resistance and can be neglected [27, 30, 39]. The boiling surface temperature T_w and the heat transfer coefficient h can be calculated as follows:

$$T_w = T_1 - q\frac{\Delta\delta}{\lambda_{Cu}} \tag{6}$$

$$h = \frac{q}{T_w - T_{sat}} \tag{7}$$

where $\Delta\delta$ is the thickness of the copper foam microchannel; T_w is the boiling surface bottom temperature; T_{sat} represents the saturation temperature of the DI water.

2.5 Uncertainty analysis

The absolute uncertainties of the T-type thermocouples were ± 0.2 °C. The thermal conductivity of copper was 395 ± 5 W/m·K with 0.1 mm uncertainty in thermocouple locations. The uncertainty of heat flux and heat transfer coefficient can be calculated using the error propagation law [40]:

$$\frac{U_q}{q} = \sqrt{\left(\frac{U_{T_1}}{T_3 - T_1}\right)^2 + \left(\frac{U_{T_3}}{T_3 - T_1}\right)^2 + \left(\frac{U_{\Delta z}}{\Delta z_{31}}\right)^2 + \left(\frac{U_{\lambda_{Cu}}}{\lambda}\right)^2} + \frac{U_{q_{loss}}}{q} \tag{8}$$

$$\frac{U_{T_w}}{T_w} = \sqrt{\left(\frac{U_{T_1}}{T_w}\right)^2 + \left(\frac{\Delta\delta}{\lambda_{Cu}T_w}U_q\right)^2 + \left(\frac{q}{\lambda_{Cu}T_w}U_{\Delta\delta}\right)^2 + \left(\frac{q\Delta\delta}{T_w\lambda_{Cu}^2}U_{\lambda_{Cu}}\right)^2} \tag{9}$$

$$\frac{U_h}{h} = \sqrt{\left(\frac{U_q}{q}\right)^2 + \left(\frac{U_{T_w}}{T_w - T_{sat}}\right)^2 + \left(\frac{U_{T_{sat}}}{T_w - T_{sat}}\right)^2} \tag{10}$$

There is a 1.2% uncertainty in the thermal conductivity of copper. In this study, thermal conductivity of PTFE and ceramic insulating material is 0.25 W/(m·K) and

0.14 W/(m·K), respectively. Through measuring the temperature difference between internal surface and outside surface of thermal insulating material (PTFE and ceramic insulating material), the heat loss (q_{loss}) can be calculated by the Fourier heat conduction equation. And the heat loss in this work is less than 4%. **Figure 5** shows the variation of the uncertainty against the heat flux on the Cu plain surface. It is seen that as the heat flux increases, the uncertainty gradually decreases [41]. And the uncertainty decreases from 20.1% to 6.3%. With a CHF of 42.1 W/cm^2, the calculated uncertainty of h and T_w is 9.2% and 6.7%, respectively.

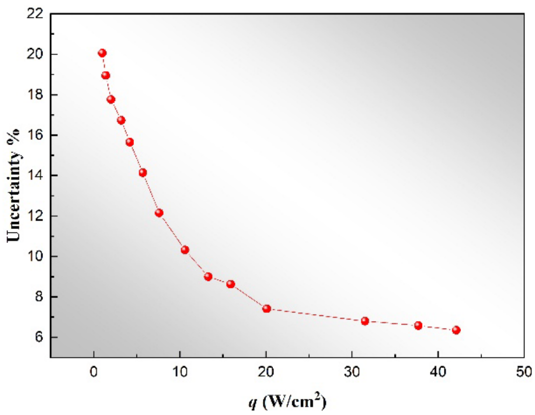

Figure 5. Variation of the uncertainty against the heat flux.

3. Results and discussions

3.1 Surface characterization

Figure 6a and **b** shows micro/nanostructures on the copper foam surfaces, respectively. Due to larger specific surface area and more nucleation sites, copper foam can enhance pool boiling heat transfer. As shown in **Figure 6a**, dense nanograss grows at an incline on the copper foam substrate after 10 immersion minutes, which is beneficial for capillary pumping improvement. After 30 immersion minutes, the nanograss tips begin to intertwine with each other and create the new crystal nucleus (**Figure 6b**). The hierarchical micro-flower and nanograss structures can provide more pores during boiling process. Pores of super-hydrophobic micro/nanostructures can capture more gas, facilitating bubble nucleation during pool boiling process.

Figure 6c – e shows the contact angle of the untreated copper foam, super-hydrophilic copper foam and super-hydrophobic copper foam. As shown in **Figure 6c**, the contact angle of untreated copper foam is around 127°. After the surface oxidation, the contact angle of the copper foam wall and bottom is 0° (**Figure 6d** and **e**), which indicates that the nanograss on the copper foam is super-hydrophilic. Further increasing 30 immersion minutes and modifying with the PTFS, the hierarchical micro-flower and nanograss structures becomes super-hydrophobic, resulting in the contact angle of 150.2° and 150.3° on the copper foam wall and bottom (**Figure 6f** and **g**), respectively. The super-hydrophilic copper foam wall can be welded onto the super-hydrophobic copper foam bottom (**Figure 6d**). On the contrary, the super-hydrophobic copper foam can be welded on the super-hydrophilic copper foam bottom (**Figure 6f**). Herein, copper foam channel with heterogeneous wetting properties can be fabricated with the immersion and weld technologies. **Table 1** shows the test copper foam samples investigated in this study.

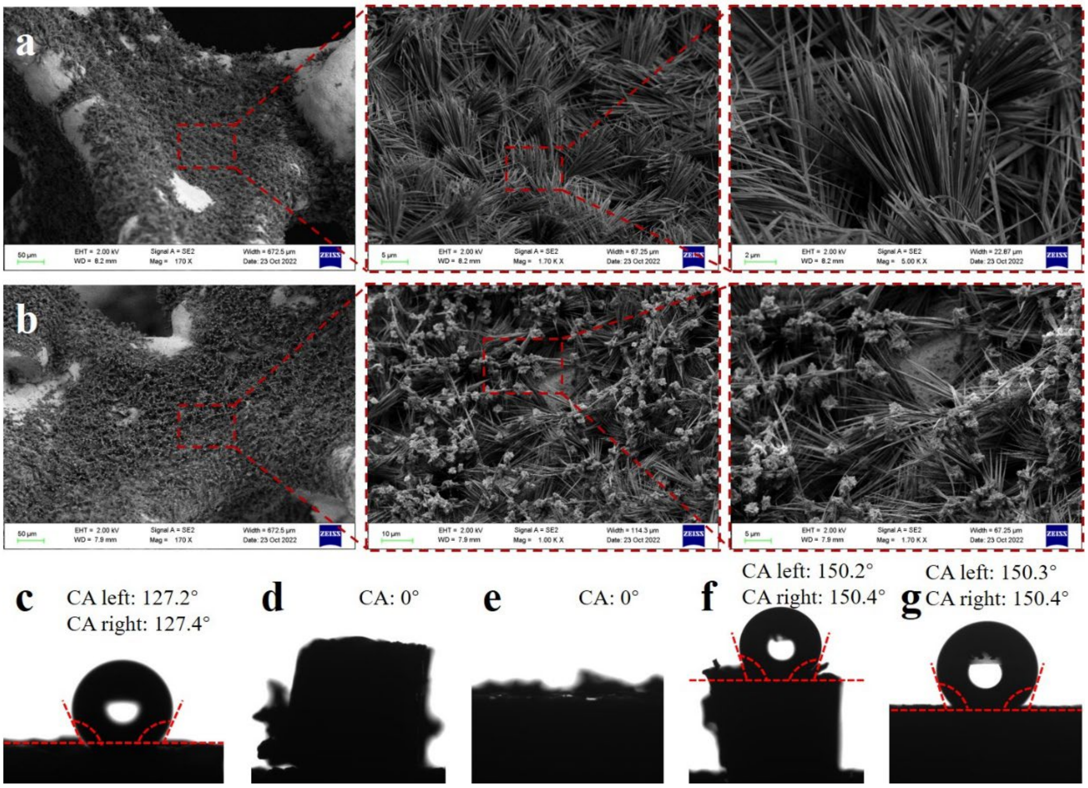

Figure 6. SEM images of (a) Super-hydrophilic micro/nanostructures (b) Super-hydrophobic micro/nanostructures; Contact angles of (c) Untreated copper foam (d) Super-hydrophilic copper foam wall (e) Super-hydrophilic copper foam bottom (f) Super-hydrophobic copper foam wall (g) Super-hydrophobic copper foam bottom.

Table 1. Characterizations of test copper foam samples (40 PPI, 5 mm).

Sample name	Structure	Channel depth (mm)	Channel width (mm)	Surface wettability
UTP	Plain	0	0	Untreated
SHPiP	Plain	0	0	Super-hydrophilic
SHPoP	Plain	0	0	Super-hydrophobic
UTM	Microchannel	2.5	2	Untreated
SHPiM	Microchannel	2.5	2	Super-hydrophilic
SHPoM	Microchannel	2.5	2	Super-hydrophobic
SHPiW-SHPoB	Microchannel	2.5	2	Super-hydrophilic wall –

				super-hydrophobic bottom
SHPoW-SHPiB	Microchannel	2.5	2	Super-hydrophobic wall – super-hydrophilic bottom

3.2 Experimental system verification

The pool boiling experiments of copper plain surface were carried out in comparison with earlier correlations and literatures to assess the verification of the pool boiling experiment system [42-48]. Typically, pool boiling performance can be estimated by three correlations. The Rohsenow's correlation can be expressed as follows:

$$\frac{c_{p,f}\Delta T_{sat}}{h_{fg}} = C_{sf}\left[\frac{q^{'}}{\mu_f h_{fg}}\sqrt{\frac{\sigma}{g\left(\rho_f-\rho_g\right)}}\right]^{0.33}\left(\frac{c_{p,f}\mu_f}{k_f}\right)^{n} \tag{11}$$

where $C_{s,f}$ = 0.0152 and n = 1, and Pioro's correlation can be expressed as:

$$\frac{q^{'}}{\Delta T_{sat}k_f}\sqrt{\frac{\sigma}{g\left(\rho_f-\rho_g\right)}} = C_{sf+}\left\{\frac{q^{'}}{h_{fg}\rho_g^{1/2}\left[\sigma g\left(\rho_f-\rho_g\right)\right]^{1/4}}\right\}^{2/3}\left(\frac{c_{p,f}\mu_f}{k_f}\right)^{m} \tag{12}$$

where C_{sf+} = 1228 and m = -1.1. The Zuber's correlation is usually estimated for the CHF value, which can be expressed as follows:

$$q_{CHF}^{'} = \frac{\pi}{24}\rho_g h_{fg}\left[\frac{\sigma g\left(\rho_f-\rho_g\right)}{\rho_g^2}\right]^{1/4} \tag{13}$$

Figure 6 presents the boiling curves obtained in this study, alongside established empirical correlations and data from the literature. At heat flux levels below 10 W/cm², the experimental results align well with the predicted values from the correlations. However, the smooth copper surface tested in this work exhibits a noticeably lower critical heat flux (CHF) compared to the values predicted by the correlations. Traditionally, Zuber's correlation has been used to estimate CHF around 100 W/cm² without accounting for surface characteristics. In practice, parameters such as surface wettability, roughness, morphology, and thermal conductivity play a critical role in determining CHF. To address the influence of surface wettability, Kandlikar proposed a modified correlation that incorporates these effects. This correlation is expressed as follows [49]:

$$q_{CHF}^{'} = h_{fg}\rho_v^{0.5}\left[\sigma g\left(\rho_l-\rho_v\right)\right]^{1/4}\frac{1+\cos\theta}{16}\left[\frac{2}{\pi}+\frac{\pi}{4\left(1+\cos\theta\right)}\right]^{0.5} \tag{14}$$

As shown in **Figure 7**, the boiling curves on the plain copper surface exhibit good repeatability, and the average CHF value from the three repeated experiments is used as a benchmark. When incorporating a contact angle of 109° into Kandlikar's correlation, the predicted CHF is 47.7 W/cm², which is slightly higher than the experimentally measured average value of 42.1 W/cm². For comparison, previous studies have reported CHF values for similar surfaces ranging from 20 to 65 W/cm². In this study, the discrepancy between the predicted and measured CHF values can be attributed to variations in surface wettability and roughness. However, the consistency of the repeated experiments validates the reliability of the data obtained from the experimental setup.

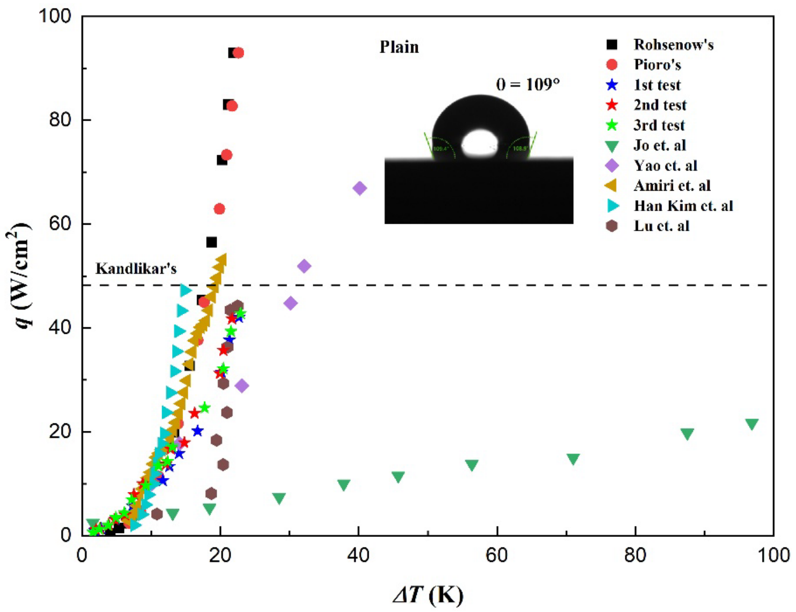

Figure 7. Boiling curve of this work and references with DI water (plain copper surfaces) [42-48].

3.3 Wettability effect on boiling performance

Figure 8 illustrates the boiling curves, heat transfer coefficient and ONB of various plain, untreated copper foam (UTP), super-hydrophilic copper foam (SHPiP) and super-hydrophobic copper foam (SHPoP) in three repeated experiments, respectively. As shown in **Figure 8a**, three boiling curves of plain, UTP and SHPoP surfaces have a good repeatability, which indicates that pool boiling performance of plain and UTP can be used as a benchmark. Due to extended surface area and increased nucleation sites, UTP exhibits a better pool boiling performance comparing to that of plain surface. The average CHF of UTP in three repeated experiments is 66.3 W/cm^2, which is 57.4% higher than that of plain surface. In comparisons, the average CHF of SHPoP is approximately 72.1% higher than that of plain surface, reaching approximately 72.1 W/cm^2. It is noted that three repeated boiling curves of plain surface have a slightly low slope (HTC), maintaining nearly unchanged, when wall superheat is lower than 7.3 K (**Figure 8a**). However, when wall superheat is higher than 7.3 K, the slope of plain surface begins to rise sharply, which suggests that HTC of plain surface increases sharply. This is attributed to the fact that heat transfer on the plain surface has started to enter the nucleate boiling regime. During two-phase nucleate boiling, bubbles nucleating and departing from the plain surface can remove significantly more heat compared to single-phase heat transfer, particularly when the wall superheat is below 7.3 K. Herein, the ONB of plain surface is around 7.3K. Different from the plain surface, UTP, SHPiP and SHPoP has a sharp rise (HTC) at the beginning, which indicates that nucleate boiling happens on UTP, SHPiP and SHPoP nearly without any waiting time (**Figure 8a**).

As shown in **Figure 8b**, both SHPiP and SHPoP surfaces exhibit significantly higher heat transfer coefficients (h) compared to the untreated plain surface (UTP). Notably, SHPoP achieves the highest heat transfer coefficient at low heat fluxes (below approximately 35 W/cm^2) across all three repeated experiments. This enhancement is attributed to the increased number of nucleation sites and more frequent bubble departure on the SHPoP surface, which facilitates efficient heat removal [30]. However, at higher heat fluxes, bubble coalescence on SHPoP leads to the formation of larger vapor bubbles that tend to blanket the surface. Due to its lower surface energy, SHPoP inhibits bubble detachment, thereby increasing interfacial thermal resistance as a vapor film forms. Consequently, the heat transfer coefficient on SHPoP declines sharply at elevated heat fluxes.

However, unlike UTP and SHPoP, SHPiP has a large variation of boiling curves in three repeated experiments (**Figure 8a**). Moreover, *h* of SHPiP in three repeated decreases slowly at a high heat flux when heat flux is higher than 35 W/cm^2, as shown in **Figure 8b**. Also, the CHF value decreases step by step after each test (**Figure 8a**). This phenomenon can be explained by the fact that SHPiP exhibits the spontaneous hydrophilicity degradation to influence bubble behaviors, resulting in the weakened pool boiling performance [50]. After being tested in second and third time, SHPiP has lost its super-hydrophilicity and become hydrophobic [51]. Herein, *h* of SHPiP sharply decreases similar to that of SHPoP at a high heat flux when heat flux is higher than 35 W/cm^2. Therefore, the surface wettability of SHPiP plays a critical role in sustaining effective pool boiling performance.

To summarize, SHPoP demonstrates the highest heat transfer coefficient at low heat flux, while SHPiP achieves superior peak performance during the initial test. After being tested in the repeated experiments, SHPiP exhibits a pool boiling performance similar to SHPoP due to hydrophilicity degradation.

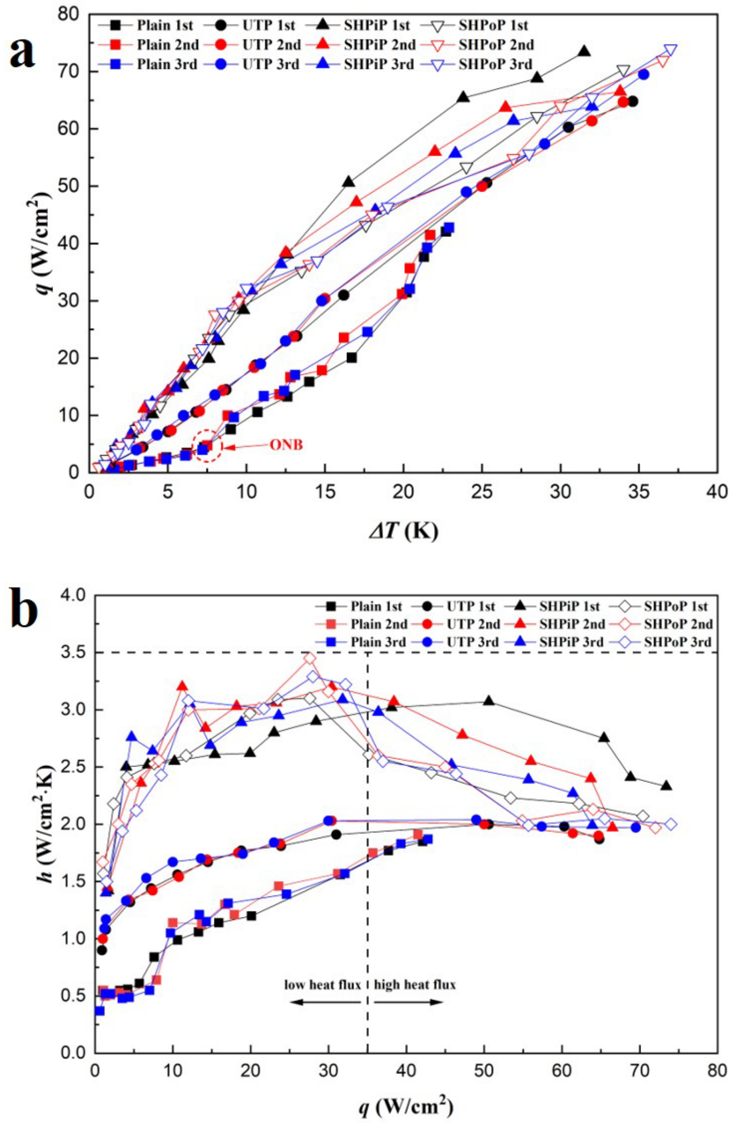

Figure 8. Wettability effect on copper foam's boiling performance in three repeated experiments (a) Boiling curves (b) Heat transfer coefficient h vs heat flux q.

3.4 Combined effects of wettability and microchannel

Figure 9 shows the three repeated boiling curves and HTCs for the UTP, UTM, SHPiM, SHPoM, SHPoW-SHPiB and SHPiW-SHPoB surfaces. Unlike UTP surface, UTM, SHPiM, SHPoM, SHPoW-SHPiB and SHPiW-SHPoB have better pool boiling performance. As shown in **Figure 9a**, similar to above-mentioned UTP surface, at the beginning, UTM, SHPiM, SHPoM, SHPoW-SHPiB and SHPiW-SHPoB have a sharp rise without any waiting time for bubble nucleation. With further increasing of the heat flux, the wall superheat of UTP, UTM, SHPiM and SHPoM copper foams continues to increase step by step. Nevertheless, SHPoW-SHPiB and SHPiW-SHPoB exhibit a sharp rising boiling curve with a small superheat. This may be caused by the fact that sufficient bubble nucleation sites on SHPoW-SHPiB and SHPiW-SHPoB can maintain nucleate boiling for a longer time. With full development of nucleate boiling, wall superheat has no significant rise as the heat flux increases, which indicates that heat can be efficiently dissipated using SHPoW-SHPiB and SHPiW-SHPoB with a small temperature rise.

As shown in **Figure 9a**, the UTP, UTM, and SHPoM surfaces exhibit good repeatability across repeated experiments, with average critical heat flux (CHF) values of 66.3 W/cm^2, 75.2 W/cm^2, and 80.2 W/cm^2, respectively. The presence of a vapor channel in UTM effectively reduces bubble escape resistance, leading to significant improvements in both CHF and heat transfer coefficient (HTC). **Figure 9b** illustrates that SHPoM demonstrates a sharp increase in HTC at heat fluxes below 25 W/cm^2. This enhancement is attributed to the increased number of bubble nucleation sites resulting from the combined effects of vapor channels and superhydrophobic surface modification. However, at heat fluxes above 25 W/cm^2, a pronounced decline in HTC is observed due to the formation of an insulating vapor film.

As shown in Figure 9a, in the initial experiment, tailoring the wettability patterns of copper foam microchannel surfaces resulted in further improvements in critical heat flux (CHF), reaching 96.1 W/cm^2 for the SHPoW–SHPiB configuration and 106.3 W/cm^2 for the SHPiW–SHPoB configuration. As reported, bubble expansion and bubble coalescence can be manipulated by the micro-posts with mixed-wettability [52]. For the SHPiW-SHPoB copper foam surface, the super-hydrophilic wall in this work plays a role similar to the micro-posts performed by Jo et. al [52], delaying the bubble coalescence at a high heat flux to further increase the CHF. However, similar to SHPiP surface, SHPiM, SHPoW-SHPiB and SHPiW-SHPoB also have a large variation of boiling curves in three repeated experiments. As shown in **Figure 9a**, the CHF value of SHPiM, SHPoW-SHPiB and SHPiW-SHPoB also decreases step by step after each test. As aforementioned, this decline in CHF may be attributed to the spontaneous degradation of surface hydrophilicity. The CHF of SHPiM decrease from 84 W/cm^2 to 74 W/cm^2 after three repeated experiments. And the CHF of SHPoW-SHPiB decreases from 96.1 W/cm^2 to 82 W/cm^2, while the CHF of SHPiW-SHPoB decreases from 106.3 W/cm^2 to 90.4 W/cm^2.

As shown in **Figure 9b**, in the first experiment, the SHPoW-SHPiB and SHPiW-SHPoB exhibit homogeneous wetting properties, allowing for a significant increase in the HTCs when compared to SHPiM and SHPoM. The maximum HTC of SHPoW-SHPiB and SHPiW-SHPoB is significantly higher (5.40 $W/cm^2 \cdot K$ and 6.14 $W/cm^2 \cdot K$). As a result, SHPoW-SHPiB and SHPiW-SHPoB can enhance boiling heat transfer by strengthening micro-convection between the released bubbles and the rewetting liquid [53-55]. There is no significant decrease in the HTC on the SHPiW-SHPoB copper foam, suggesting the nucleate boiling can be maintained on this copper foam structure. Meanwhile, the SHPiW-SHPoB can display a higher HTC compared wtih SHPoW-SHPiB. This indicates that heterogeneous wettability can remarkably affect boiling heat transfer, and heterogeneous wettability with different patterns can further increase the HTC of copper foam microchannels. As shown in **Figure 9b**, h of SHPiM decreases sharply in the third experiment. Besides, as shown in **Figure 9b**, SHPoW-SHPiB and SHPiW-SHPoB also exhibits a sharp decline of h when heat flux is higher than about 60 W/cm^2 in the second and third experiment. This is also attributed to the fact that spontaneous hydrophilicity degradation on SHPoW-SHPiB and SHPiW-SHPoB increase bubble escape resistance, resulting in decreased h at a high heat flux.

For evaluating pool boiling performance of copper foam with vapor channels in this work, some similar works with pool boiling enhancement using enhanced copper foam structures are listed in **Table 2**. Besides, HTC_{foam}/HTC_{plain} and CHF_{foam}/CHF_{plain} are defined to evaluate pool boiling heat transfer comparing to the previous studies. Here, HTC_{foam}, HTC_{plain}, CHF_{foam} and CHF_{plain} represents the HTC of copper foam, HTC of smooth surface, CHF of copper foam and CHF of smooth surface, respectively. Due to the hydrophilicity degradation, the CHF and HTC decreases after repeated experiments. As a result, we conducted the same pool boiling experiments on three SHPoW-SHPiB surfaces and SHPiW-SHPoB surfaces with one time test to illustrate the effect of copper foam with different wetting vapor channels on pool boiling performance. As shown in **Figure 10**, the average CHF of SHPoW-SHPiB and SHPiW-SHPoB is 96.7 W/cm^2 and 108.2 W/cm^2, respectively. And the average maximum HTC of SHPoW-SHPiB and SHPiW-SHPoB is 5.56 W/cm^2·K and 6.25 W/cm^2·K. As listed in **Table 2**, comparing with the plain surface, treated copper foam structures can enhance the CHF and HTC dramatically. Through wettability modification, the CHF and HTC can be improved to a certain extent [28-30]. Using copper foam manufactured with Magnetron sputtering and electrodeposition, the CHF and HTC can also be improved [56, 57]. Moreover, using copper foam with multilayer pore density gradient, CHF can be increased and the CHF_{foam}/CHF_{plain} increases to 2.13 [34]. Using copper foam with vapor channel, the HTC can be dramatically improved and the HTC_{foam}/HTC_{plain} is 2.5 [57]. Comparing with the previous works, through copper foam with heterogeneous wetting vapor channels, the CHF and HTC simultaneously have a significant improvement. In this work, on SHPoW-SHPiB, the CHF_{foam}/CHF_{plain} is 2.3, while the HTC_{foam}/HTC_{plain} is 2.9. Furthermore, on SHPiW-SHPoB, the CHF_{foam}/CHF_{plain} increases to 2.57 and the HTC_{foam}/HTC_{plain} reaches 3.34. Therefore, pool boiling performance can be improved significantly using copper foam with heterogeneous wetting vapor channels, especially using SHPiW-SHPoB structure.

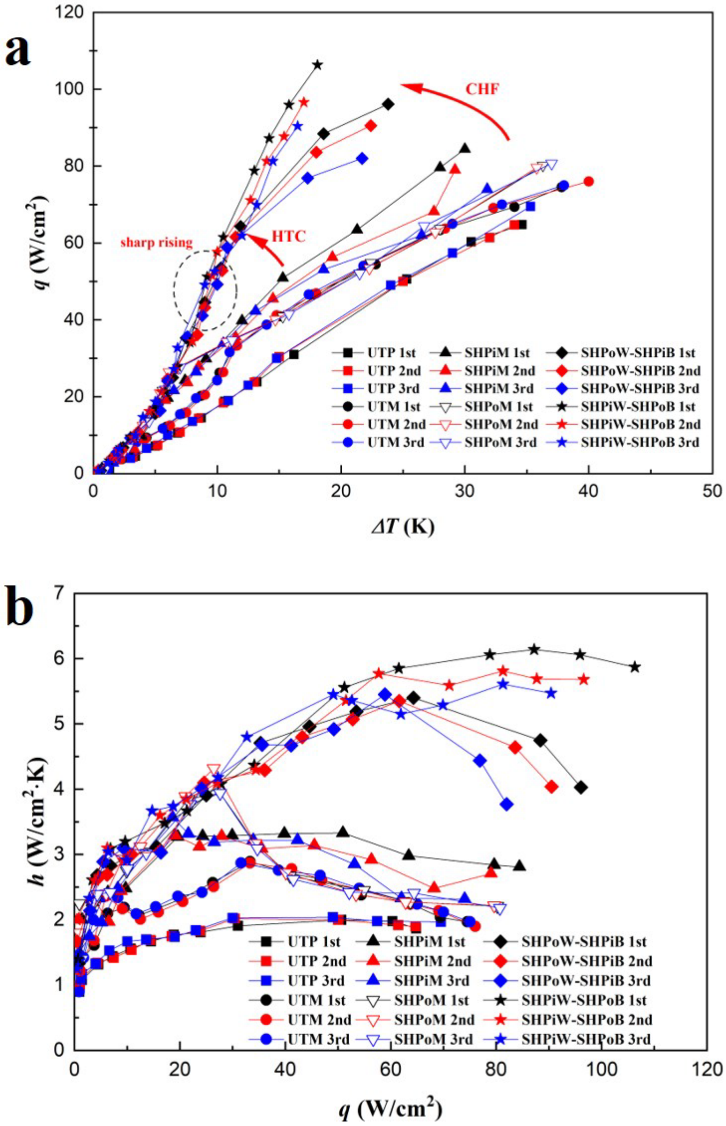

Figure 9. Effects of wettability and microchannel on copper foam's boiling performance (a) boiling curves (b) Heat transfer coefficient *h* vs heat flux *q*

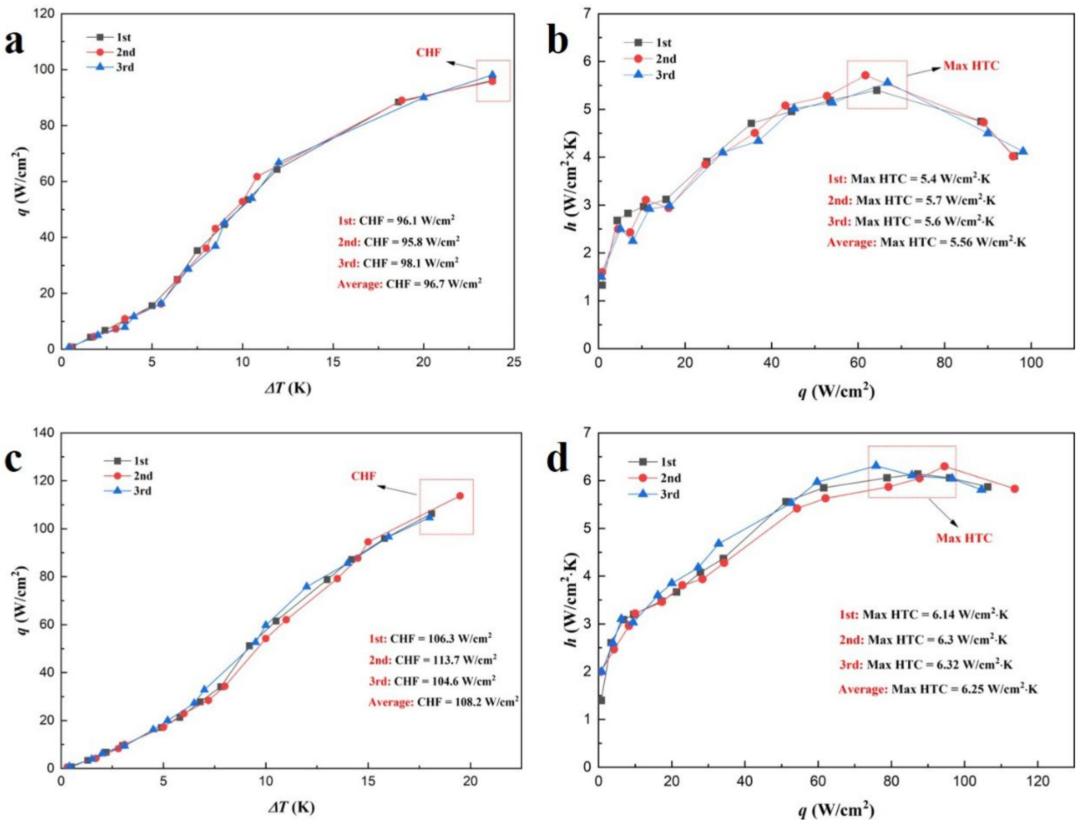

Figure 10. CHF and Max HTC of three SHPoW-SHPiB and SHPiW-SHPoB samples (a) CHF of SHPoW-SHPiB (b) HTC of SHPoW-SHPiB (c) CHF of SHPiW-SHPoB (d) HTC of SHPiW-SHPoB.

Table 2. Pool boiling performance comparisons on copper foam structures with previous works.

Ref.	Structure	Working fluid	CHF_{foam}/CHF_{plain}	Max HTC_{foam}/Max HTC_{plain}
Shi et.al [30]	Super-hydrophilic copper foam	DI water	1.05	1.18
Hu et. al [29]	Hydrophobic copper foam	DI water	1.11	1.3
Huang et. al [34]	Multilayer gradient copper foam	DI water	2.13	/
Sharifzadeh et. al [31]	Copper foam with one channel	DI water	1.5	2.5
Yao et. al [56]	Magnetron sputtering copper foam	DI water	1.1	1.25
Sharifzadeh et. al [57]	Electrodeposited copper foam	DI water	1.22	1.84
Hu et. al [28]	Hydrophilic copper foam	DI water	1.46	1.3

This work 1	SHPoW-SHPiB	DI water	2.3	2.97
This work 2	SHPiW-SHPoB	DI water	2.57	3.34

3.5 Bubble behavior visualization

3.5.1 Bubble nucleation

Figure 11 shows wall superheat at ONB in the first and third boiling tests. In the first test, the order of ΔT_{ONB} is as follows: Plain > UTP > UTM > SHPiP > SHPiM > SHPoP > SHPoM > SHPoW-SHPiB > SHPiW-SHPoB. **Figure 12** illustrates the number of bubbles attached to the copper foam surfaces at ONB during the first test. Compared to UTP (**Figure 12a**), more bubbles are observed on SHPoP (**Figure 12c**). The micro/nano-structured surface of SHPoP effectively traps gas (**Figure 12c**), facilitating the activation of more nucleation sites. Consequently, SHPoP exhibits significantly higher heat transfer efficiency than UTP **(Figure 8b)**. In contrast, the super-hydrophilic nature of SHPiP allows liquid to readily penetrate its porous structure, reducing residual gas pockets. This results in a higher energy barrier for bubble nucleation [30]. These observations are consistent with Hsu's theory [58], which is depicted as:

$$\begin{Bmatrix} r_{eff,\min} \\ r_{eff,\max} \end{Bmatrix} = \frac{\delta_t \sin\theta}{2\left(1+\cos\theta\right)}\left[1 \mp \sqrt{1-\frac{8\sigma T_{sat}\left(1+\cos\theta\right)}{\rho_v h_{fg}\delta_t \Delta T_w}}\right] \quad (15)$$

where δ_t, θ, σ, ρ_v, and h_{fg} are the thermal boundary layer thickness, contact angle, surface tension, vapor density and latent heat of vaporization, respectively. T_{sat} and T_w are the saturated temperature and wall superheat. The active nucleation sites size range can be expanded by increasing the contact angle according to Eq. (15). Hence, except more captured gas, more pores with suitable size can be used as active nucleation sites on the SHPoP. In contrast, UTP exhibits fewer bubbles since only its original pores function as effective nucleation sites (**Figure 12a**). With super-hydrophilic modification, numerous pores created by micro/nano structures act as active nucleation sites on SHPiP. As a result, tiny bubbles are observed on SHPiP, indicating the formation of many effective, small-sized nucleation sites (**Figure 12b**).

Furthermore, researches exhibit that the bubbles can be easily nucleated at the corners of the microchannels [59]. This is attributed to the fact that cavitation can be easily formed at the corner. This finding is in agreement with the bubble nucleation shown in **Figure 12d**, **e**, **f**, **g** and **h**. As shown in **Figure 12f**, similar to the SHPoP, more captured gas can be obtained on the SHPoM, resulting in abundant bubble nucleation. Besides, combining above-mentioned cavitation, more bubble nucleation can be obtained on the SHPoM compared with the SHPoP. For the UTM and SHPiM, corner bubbles can be obtained due to the cavitation phenomenon. Therefore, compared to UTP and SHPiP, UTM and SHPiM offer more opportunities for bubble nucleation due to a greater number of effective nucleation sites (Figure 12d and e).

Beyond the influences of wettability and microchannel corners, researchers have observed that bubbles tend to nucleate more readily along hydrophobic boundaries [60]. On the SHPoW-SHPiB and SHPiW-SHPoB surfaces, various bubble types, such as corner bubbles, tiny bubbles, and bubbles formed from trapped gas, are commonly observed. Consequently, due to the combined effects of microchannel corners and heterogeneous wettability, these copper foams promote faster bubble nucleation (**Figure 12g and h**), requiring lower wall superheat for onset of nucleate boiling (ONB). It is noteworthy that the ONB values for SHPiP, SHPiM, SHPoP, SHPoM, SHPoW-SHPiB, and SHPiW-SHPoB are similar. This similarity arises because numerous bubbles nucleate at pores of suitable size, which serve as effective nucleation sites. Additionally, as heat flux increases, more heat is absorbed at these active nucleation sites, leading to comparable ONB values across these surfaces.

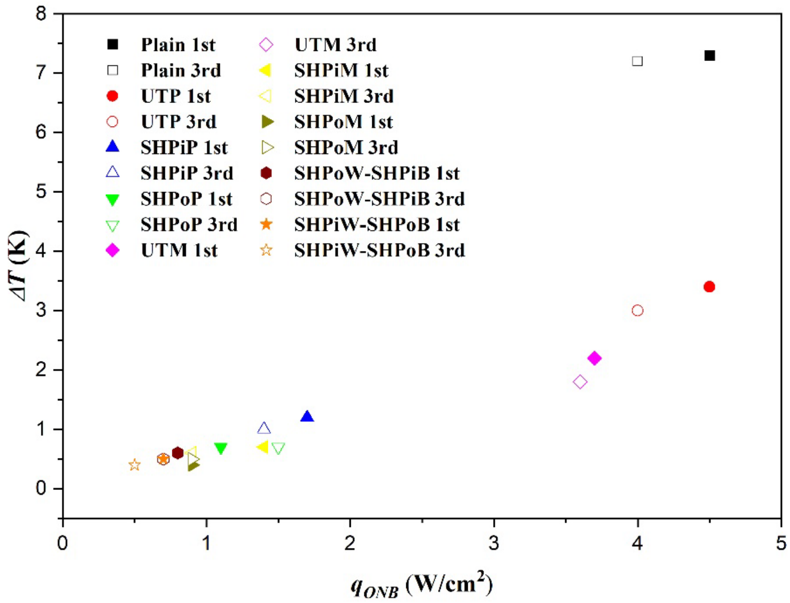

Figure 11. Wall superheat at ONB in the first and third boiling test.

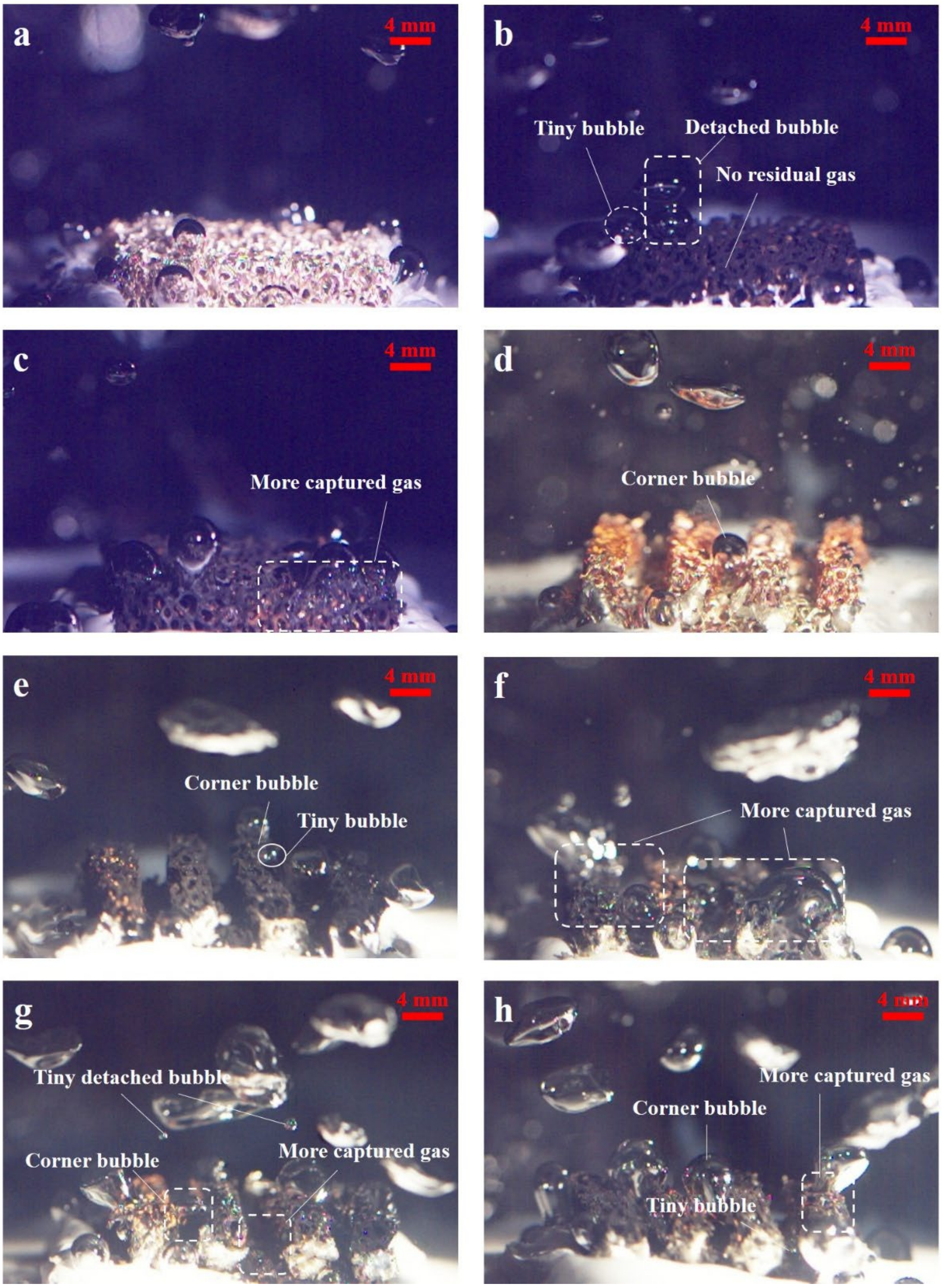

Figure 12. Bubble dynamics at ONB in the first test (a) UTP (b) SHPiP (c) SHPoP (d) UTM (e) SHPiM (f) SHPoM (g) SHPoW-SHPiB (h) SHPiW-SHPoB.

As aforementioned, due to hydrophilicity degradation, the pool boiling performance of SHPiP, SHPiM, SHPoW-SHPiB, and SHPiW-SHPoB changes noticeably after three repeated boiling tests. **Figure 13** presents the bubble dynamics at ONB for these surfaces during the third test. In contrast, bubble dynamics on UTP, SHPoP, UTM, and SHPoM remain relatively consistent between the first and third tests (as shown in **Figures 12 and 13**), which can be attributed to the stable wettability of these surfaces and no occurrence of hydrophilicity degradation, resulting in unchanged nucleation behavior. As illustrated in **Figures 13b, 13c, 13e, 13f, and 13h**, similar to the SHPoP surface, more trapped gas is observed on SHPiP, SHPiM, SHPoW-SHPiB, and SHPiW-SHPoB in the third test. This contributes to the activation of additional nucleation sites due to reduced surface wettability. Furthermore, the microchannel corner geometry offers favorable sites for cavitation, facilitating bubble nucleation. As a result, more bubbles are observed on SHPiM, SHPoW-SHPiB, and SHPiW-SHPoB compared to SHPiP (**Figures 13b, 13e, 13f, and 13h**). According to the equation as follows:

$$\cos\theta = 2\xi\left(\frac{\gamma_s}{\sigma}\right)^{1/2} - 1 \tag{16}$$

where θ is contact angle, ξ is a constant, σ is the liquid surface tension, and γ_s is surface energy. After undergoing repeated boiling tests, hydrophilicity degradation occurs on these surfaces, leading to an increased contact angle and reduced surface energy. As a result, SHPiP, SHPiM, SHPoW-SHPiB, and SHPiW-SHPoB exhibit hydrophobic behavior during the third boiling test. Consequently, the ONB (onset of nucleate boiling) for these surfaces becomes closely aligned with that of the SHPoP surface.

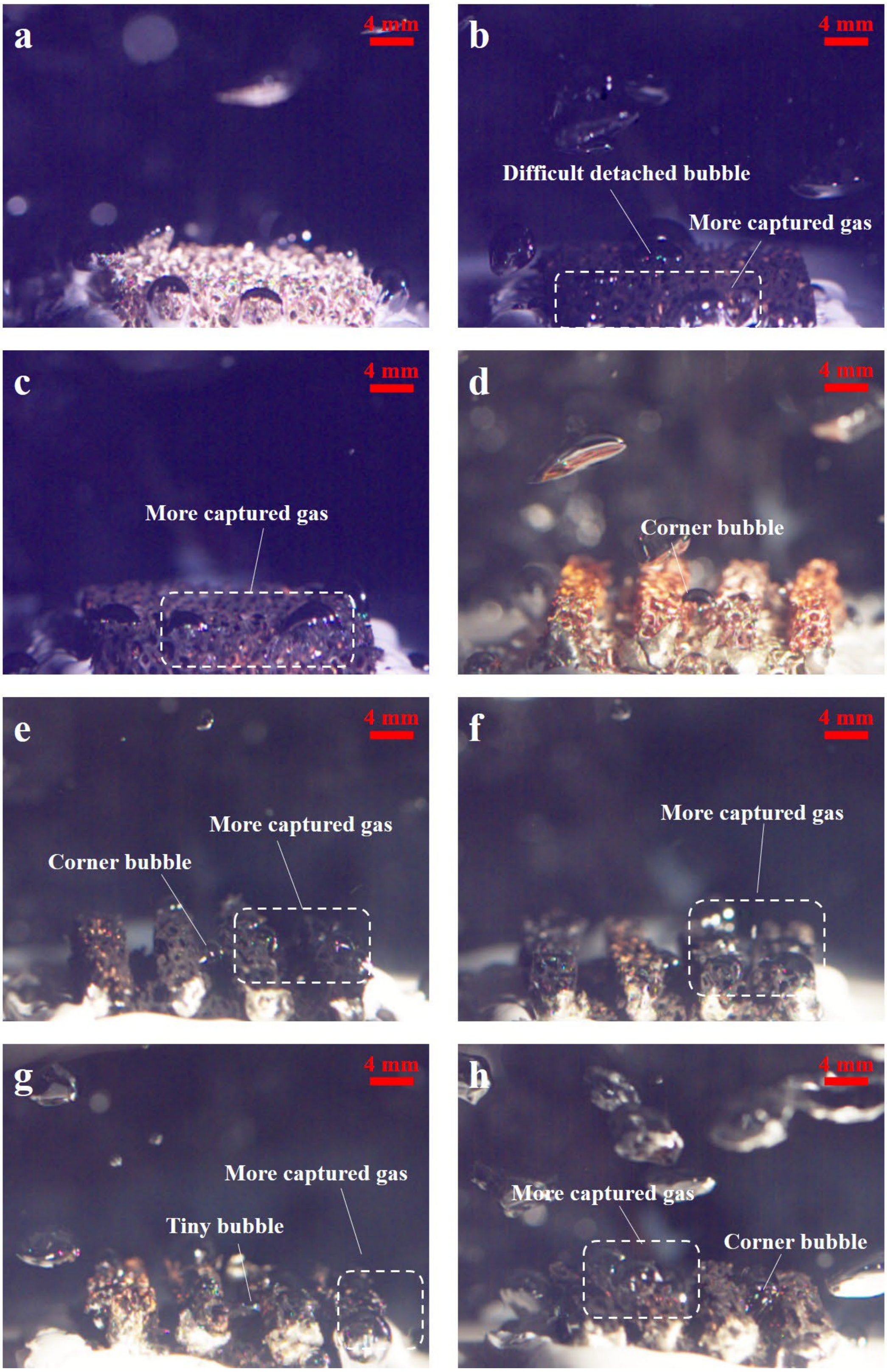

Figure 13. Bubble dynamics at ONB in the third test (a) UTP (b) SHPiP (c) SHPoP (d) UTM (e) SHPiM (f) SHPoM (g) SHPoW-SHPiB (h) SHPiW-SHPoB.

3.5.2 Bubble growth period

As shown in **Figure 14**, when the heat flux is approximately 4 W/cm², all copper foam surfaces exhibit isolated bubbles during the bubble growth phase. In general, bubble growth on the UTP is influenced by multiple forces, including contact pressure from the copper foam, surface tension, bubble escape resistance, heat flux-induced driving force, buoyancy, and bubble expansion force. Once a bubble reaches a critical radius, it detaches from the copper foam. As illustrated in **Figure 14a**, bubble departure on the UTP is followed by a waiting period of about 40 ms before the next bubble nucleates. In contrast, the super hydrophilic micro/nanostructures on SHPiP reduce the surface tension, allowing bubbles to detach more rapidly. Additionally, the next bubble nucleation occurs sooner (**Figure 14b**), due to the lower amount of captured gas and easier liquid rewetting. Compared to SHPiP, the SHPoP surface captures more gas, supplying more nucleation sites. However, the higher surface tension on SHPoP hinders the bubble detachment, resulting in a longer departure time of approximately 65 ms (**Figure 14c**). Despite of this, SHPoP demonstrates a shorter waiting time before the next bubble forms. This may be due to residual portions of previous bubbles acting as micro-nucleation sites, facilitating quicker subsequent nucleation [61].

For the copper foam microchannels, UTM can nucleate more bubbles at the corner of the microchannels, while the waiting time for the next bubble nucleation is shorter comparing with the UTP (**Figure 14d**). This is attributed to the fact that the bubbles can be nucleated more easily at the sharp corners of microchannels [59]. Comparing with the UTM, SHPiM has faster bubble departure. Nevertheless, the next bubble nucleation requires longer waiting time of 25 ms because the microchannel can facilitate the liquid to cool nucleation sites driven by the capillary pressure (**Figure 14e**). Therefore, next bubble nucleation requires more energy, leading to the longer waiting time. Herin, SHPoP also has longer waiting time for neat bubble nucleation (**Figure 14f**). Moreover, due to higher surface tension on SHPoM, difficult bubble departure appears.

As shown in **Figure 14g** and **14h**, SHPoW-SHPiB and SHPiW-SHPoB have shorter waiting time for the next bubble nucleation. However, as comparisons, SHPoW-SHPiBhas longer bubble growth period ranging from bubble nucleation to bubble departure and larger bubble size, leading to the worse pool boiling heat transfer. Overall, through using mixed wettability modification, shorter bubble growth period and waiting time through this method to enhance boiling heat transfer at low heat flux [62]. Moreover, combining mixed wettability and microchannel structures, boing heat transfer performance could be significantly due to easier bubble nucleation, shorter bubble growth period, faster bubble detachment and effortless next bubble nucleation.

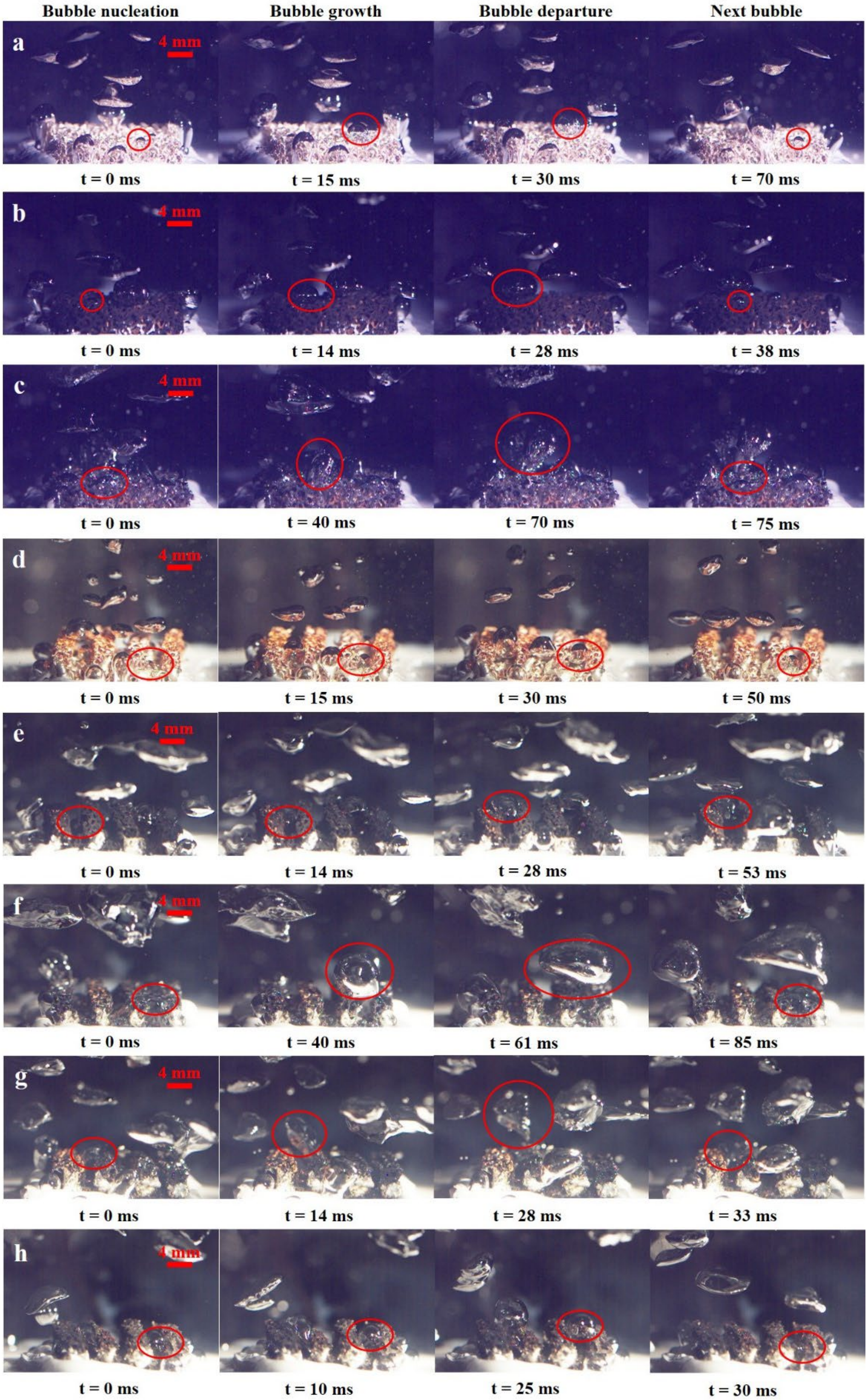

Figure 14. Bubble dynamics at $q \approx 4$ W/cm^2 (a) UTP (b) SHPiP (c) SHPoP (d) UTM (e) SHPiM (f) SHPoM (g) SHPoW-SHPiB (h) SHPiW-SHPoB.

3.5.3 Bubble departure

Figure 15 shows the bubble growth diameter (D_b) for the various copper foam samples under heat fluxes of approximately 4, 7, and 10 W/cm². Bubble grows rapidly in the initial stage due to surface tension. Subsequently, the bubble diameter growth rate decreases with time because of thermal diffusion. Here note that using the super-hydrophilic micro/nanostructure or microchannel structure can decrease the bubble departure diameter (**Figure 15b** and **d**). This is due to that super-hydrophilic micro/nanostructure or microchannel can improve capillary pressure to facilitate the bubble detachment. Thus, SHPiM copper foam can significantly increase bubble diameter growth rate (**Figure 15e**). As comparisons, with super-hydrophobic modification, bubble diameter growth rate on the SHPoP is significantly reduced due to larger surface tension (**Figure 15c**). Meanwhile, SHPoM exhibits the slightly higher growth rate. This is attributed to the fact that faster bubble detachment could be driven by strengthened capillary wicking resulting from the microchannel (**Figure 15f**). As shown in **Figure 15g** and **h**, due to the synergistic effects of microchannel and different wetting properties, SHPoW-SHPiB and SHPiW-SHPoB can significantly increase bubble diameter growth. The SHPiW-SHPoB exhibits the highest bubble diameter growth rate and smallest bubble departure diameter. According to the equation as follows:

$$HTC\alpha \frac{\rho_l h_{fg}}{D_b(T_w - T_f)} \tag{17}$$

where ρ_l and h_{fg} is the liquid density and latent heat of vaporization, respectively. HTC increases with D_b (bubble diameter) decreases. Therefore, the SHPiW-SHPoB exhibits the best boiling heat transfer at a low heat flux.

Figure 16 shows bubble departure frequency increases with an increase of heat flux. Also, owing to increased nucleation sites and shorter waiting period, SHPiW-SHPoB exhibits the highest f. Herein, when using SHPiW-SHPoB, through manipulating bubble growth period and continuous small bubble nucleation and departure, boiling heat transfer at low heat flux can be significantly improved.

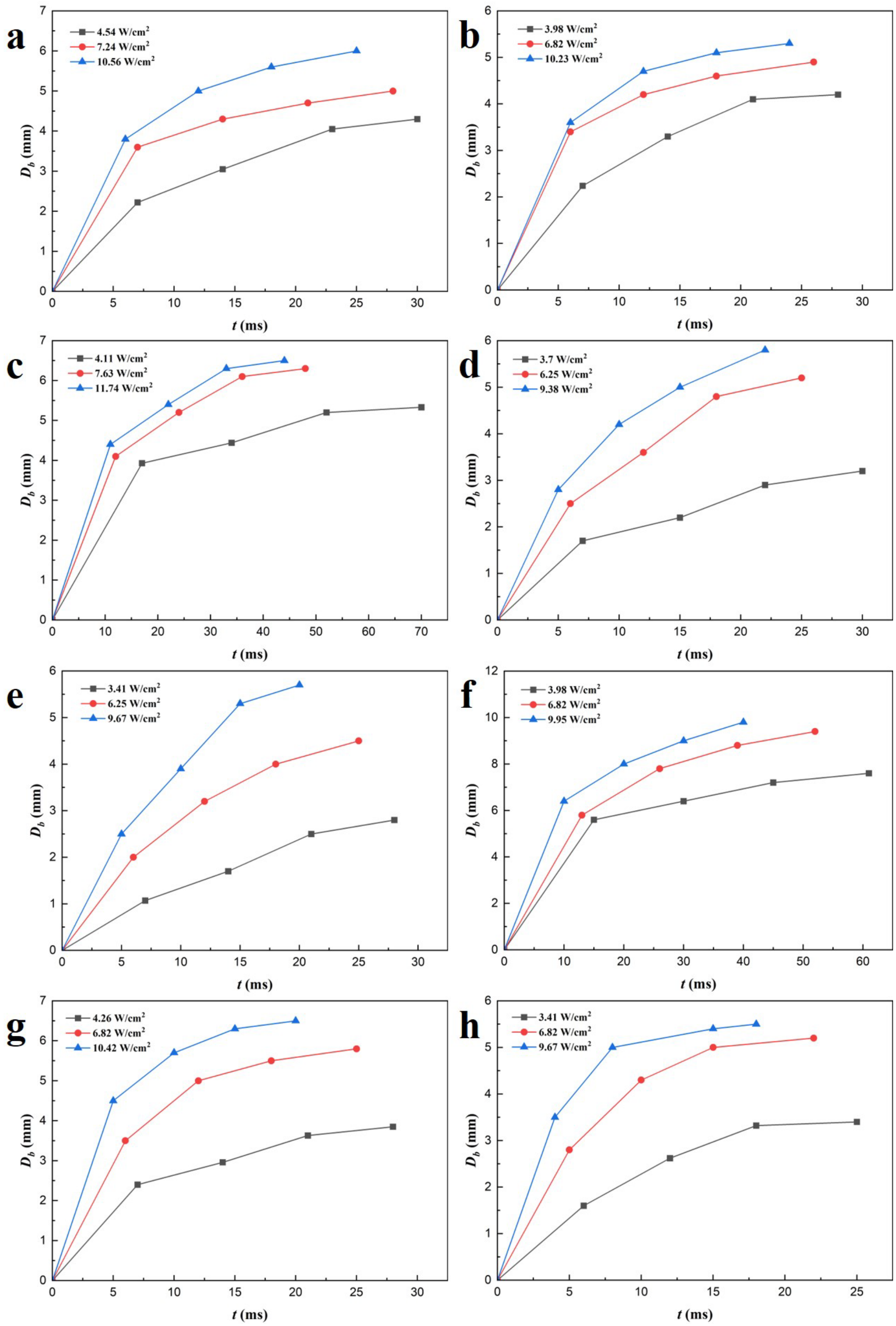

Figure 15. Bubble diameters during growth period at various heat fluxes (a) UTP (b) SHPiP (c) SHPoP (d) UTM (e) SHPiM (f) SHPoM (g) SHPoW-SHPiB (h) SHPiW-SHPoB.

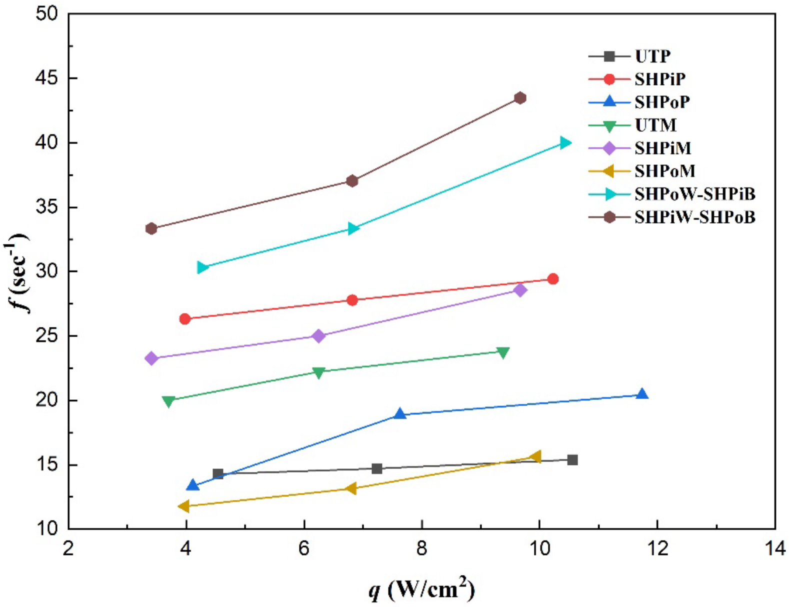

Figure 16. Bubble departure frequency for the whole samples.

3.5.4 Bubble coalescence

At high heat flux conditions, bubble coalescence can lead to the formation of a vapor film that hinders liquid replenishment, thereby deteriorating boiling heat transfer performance. **Figure 17** illustrates the bubble coalescence behavior on different copper foam surfaces under heat fluxes of approximately 30, 50, and 60 W/cm^2. As shown in **Figure 17a**, when the heat flux is 30.9 W/cm^2, aggerated large bubbles are detaching from UTP. At heat flux of 50.5 W/cm^2, vigorous lateral coalescence easily forms before detaching from UTP copper foam, leading to a decrease in boiling heat transfer. At heat flux of 60.2 W/cm^2, the mushroom bubble forms at the center of UT close to the CHF. With the super-hydrophilic modification, discrete large bubble and isolated bubble can still be observed on SHPiP at similar heat flux of 28.4 and 50.6 W/cm^2 (**Figure 17b**). At high heat flux of 65.4 W/cm^2, lateral bubble coalescence appears first at the edge of SHPiP. Meanwhile, discrete large bubbles still exist at the center of SHPiP, indicating that the liquid replenishment has been began to be inhibited. As shown in **Figure 17c**, when the heat flux is 27.6 W/cm^2, lateral bubble coalescence easily forms due to the bubble pinning resulted from larger surface tension on SHPo. The oblate-shaped bubbles can be observed at heat flux of 53.4 W/cm^2, indicating that bubbles grow rapidly in lateral direction than that in vertical direction. At heat flux of 62.2 W/cm^2, a large mushroom vapor bubble can be observed, and the remaining vapor beneath the mushroom vapor can be continuously nucleated for bubble coalescence. This behavior signifies the formation of a sustained vapor film, further degrading boiling heat transfer efficiency.

Unlike the above-mentioned plain copper foam surfaces, more distributed and discrete bubbles appear on copper foam microchannels. As shown in **Figure 17d**, distributed bubbles and discrete large bubbles exist on UTM at heat flux of 33.3 and 54.4 W/cm^2, while conical bubble can be formed at high heat flux of 63.3 W/cm^2. As comparisons, no significant bubble coalescence exists on SHPiM at heat flux of 29.9, 50.9 and 63.4 W/cm^2 (**Figure 17e**), respectively. This can be attributed to the synergistic super-hydrophilic modification and the microchannel structures. As shown in **Figure 17f**, comparing with SHPo, bubble pinning which can result in the difficult bubble departure can be also observed on SHPoM, while no continuous lateral bubble coalescence appears due to liquid supply from the channel. At heat flux of 63.7 W/cm^2, discrete conical bubbles can be observed due to the channel segmentation, indicating that liquid supply from the channel forbids the bubble coalescence.

With respect to the SHPoW-SHPiB and SHPiW-SHPoB (**Figure 17g** and **h**), more distributed bubbles and discrete bubbles can be formed due to the combined effect of heterogeneous wettability and microchannel structures. It is worth noting that bubble vapor finally escapes from super-hydrophobic copper foam microchannel top on SHPoW-SHPiB (**Figure 17g**). At heat flux of 64.3 W/cm^2, discrete large bubble can also be formed on SHPoW-SHPiB, indicating the tendency of the lateral bubble coalescence with an increase in heat flux. However, on SHPiW-SHPo (**Figure 17h**), more distributed small bubbles escape from the microchannel at heat flux of 34.1 and 51.2 W/cm^2, respectively. This is due to that liquid replenishment from super-hydrophilic microchannel top can make bubbles distributed. At heat flux of 61.6 W/cm^2, discrete bubbles are still formed using this type copper foam, indicating that the nucleate boiling has been delayed for enhancing boiling heat transfer. Although SHPiM also exhibits the discrete bubble phenomenon (**Figure 17e**) at high heat flux (63.4 W/cm^2), less bubble can be continuously nucleated. Therefore, less heat can be carried away on SHPiW. Herein, comparing with SHPiM, SHPoW-SHPiB and SHPiW-SHPo demonstrate superior boiling heat transfer. Meanwhile, through delaying nucleate boiling, SHPiW-SHPoB has better boiling heat transfer than that of SHPoW-SHPiB.

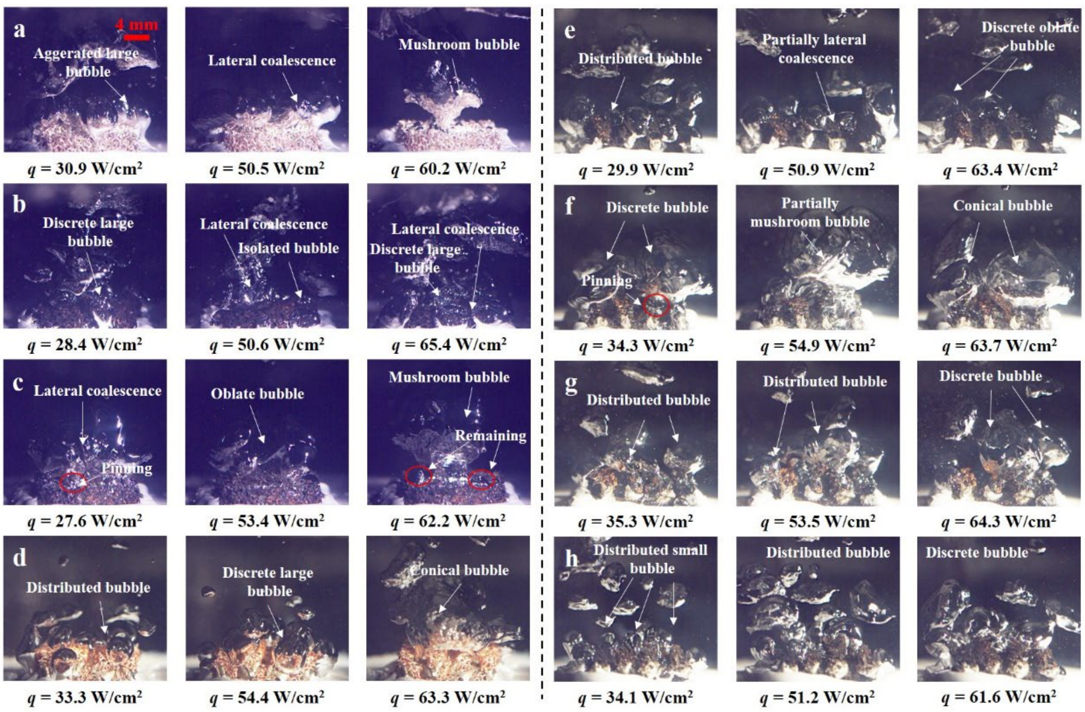

Figure 17. Bubble behavior at different heat fluxes on the samples. (a) UTP (b) SHPiP (c) SHPoP (d) UTM (e) SHPiM (f) SHPoM (g) SHPoW-SHPiB (h) SHPiW-SHPoB.

3.6 Boiling enhancement mechanism

The incorporation of heterogeneous wetting vapor channels in copper foam significantly influences pool boiling performance. These structures combine regions of differing wettability to optimize bubble nucleation, growth, and departure. By creating a controlled vapor escape pathway, the mixed-wettability design enhances liquid replenishment and delays vapor film formation, thereby improving heat transfer efficiency and increasing the critical heat flux (CHF). As previously discussed, the pool boiling performance of copper foam surfaces can be affected by repeated testing due to changes in surface properties. To better understand the boiling enhancement mechanism associated with copper foams featuring heterogeneous wetting vapor channels, a single round of pool boiling experiments was conducted on three identical surfaces. This approach isolates the initial performance characteristics and highlights the effects of the heterogeneous wetting design. **Figure 18** illustrates average boiling heat transfer coefficient ratio of modified copper foam to untreated copper foam (h/h_0). With increase of heat flux, h/h_0 of SHPiP and SHPoP exhibit a trend slight increase and then decrease, while h/h_0 of UTM, SHPiM and SHPoM exhibit a trend of significant increase and then decrease. However, as heat flux increases, h/h_0 of SHPoW-SHPiB and SHPiW-SHPoB constantly increases. According to the above-mentioned analysis in **Figure 17b** and **c**, increased vapor resistance resulting from significant lateral bubble coalescence and partial vapor layer on SHPiP and SHPoP can slow bubble escape at a high heat flux. As heat flux increases, distributed or discrete bubbles can be maintained for longer time using UTM, SHPiM and SHPoM (**Figure 17d**, **e** and **f**). This is achieved by lowering the bubble escape resistance, which causes a rapid bubble release at low heat flux. The h/h_0 drops sharply for the UTM and SHPoM because the lateral bubble coalescence can still be observed at high heat flux. Bubbles are difficult to run away quickly due to increased vapor resistance. However, due to the abundant liquid replenishment, more discrete bubbles still exist on SHPiM at high heat flux, h/h_0 slightly decreases. As shown in **Figure 17g** and **h**, continuous bubble release can be obtained on SHPoW-SHPiB and SHPiW-SHPoB (**Figure 17g** and **h**), leading to h/h_0 of 3. Developed nucleate boiling is maintained to cause h/h_0 to continuously rise.

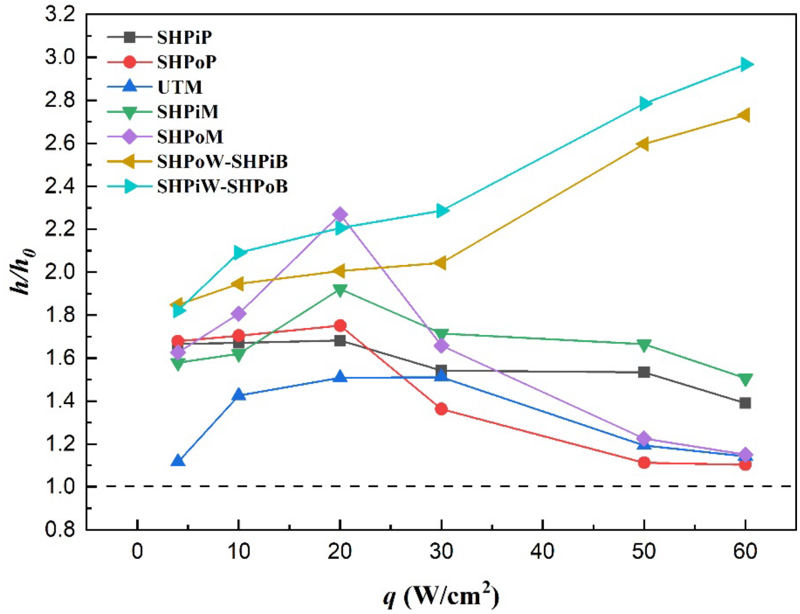

Figure 18. Boiling heat transfer ratio (h/h_0) of all the copper foam surfaces at different heat fluxes.

As shown in **Figure 19c**, heterogeneous wettable copper foam microchannels can separate liquid-vapor phases, which lowers the resistance to release bubbles and strengthens the capillary pumping to drive liquid rewetting [31, 32]. In addition, further modified with the heterogeneous wettability, more nucleation sites can be provided by the microchannel conner and hydrophobic areas, while super-hydrophilic copper foam can invoke a large positive pressure for improving liquid replenishment [30]. Using heterogeneous wettability and copper foam microchannel, separation of liquid supply and vapor removal can be formed to enhance boiling heat transfer. Nevertheless, bubbles escape from SHPiW-SHPoB copper foam microchannel (**Figure 19a**) and from SHPoW-SHPiB copper foam top (**Figure 19b**). This is attributed to the fact that bubbles can easily nucleate at the foam microchannel corner and super-hydrophobic foam bottom on the SHPiW-SHPoB, and super-hydrophilic foam can facilitate bubble departure due to liquid replenishment (**Figure 19a**). On SHPoW-SHPiB copper foam, vapor remaining can promote next bubble nucleation to improve nucleate boiling. Nevertheless, too more vapor remaining can be captured by super-hydrophobic foam wall can prevent the liquid replenishment to further improve boiling heat transfer (**Figure 19b**). Noting that bubble escape resistance increases on SHPoW-SHPiB copper foam because of higher surface tension, resulting in the slower bubble release than that of the SHPiW-SHPoB copper foam.

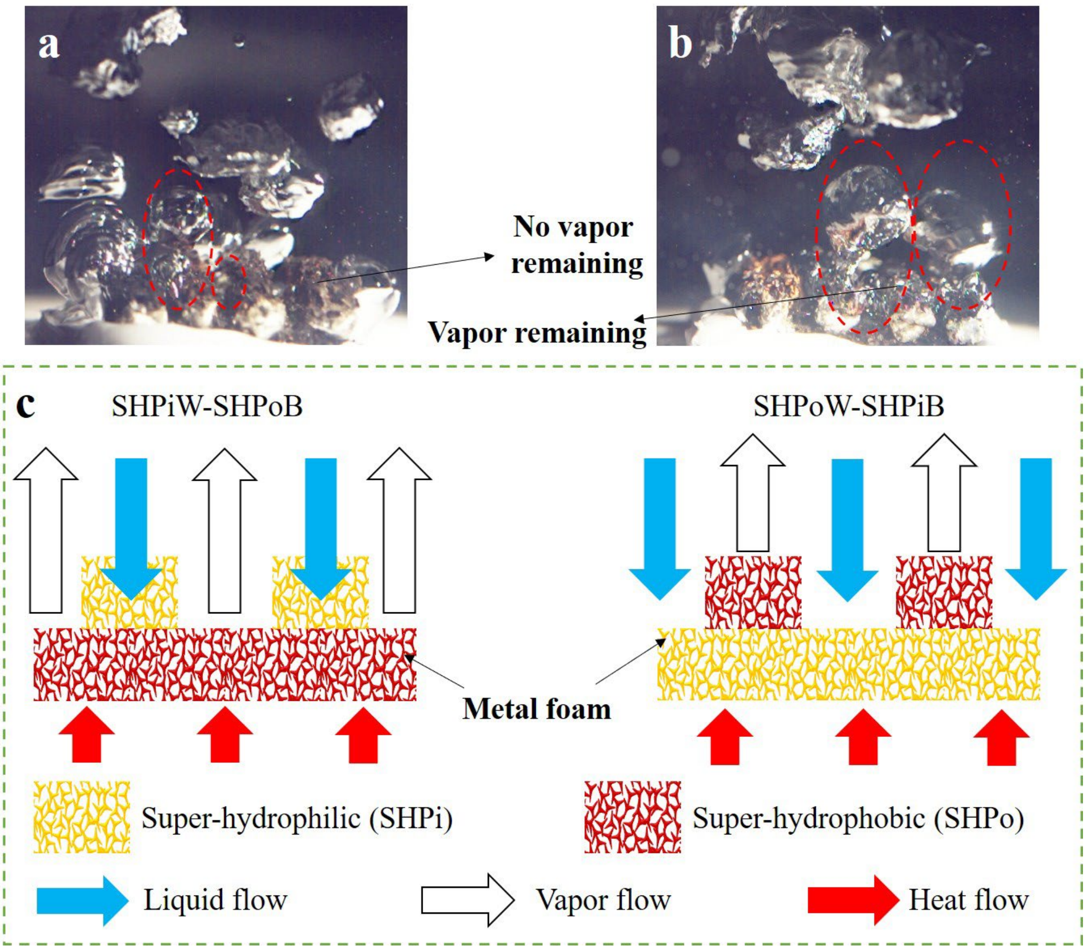

Figure 19. (a) bubble escape on the SHPiW-SHPoB (b) bubble escape on the SHPoW-SHPiB (c) schematic of liquid-vapor separation on the SHPiW-SHPoB and SHPoW-SHPiB copper foams.

Hydrophilicity degradation refers to the gradual loss of surface wettability after repeated boiling cycles. This degradation leads to an increase in contact angles and a reduction in surface energy, transforming initially super-hydrophilic surfaces into hydrophobic ones. As a result, bubble dynamics change and nucleation becomes easier due to more trapped gas, but liquid replenishment is hindered, which can lower boiling performance and reduce critical heat flux (CHF) over time. In this section, three repeated experiments using the same boiling surface were conducted to explore the hydrophilicity degradation effect on pool boiling performance. As aforementioned, after three repeated pool boiling experiments, SHPiP, SHPiM, SHPiW-SHPoB and SHPoW-SHPiB suffer destruction to lose their hydrophilicity, resulting in weakening pool boiling performance. As shown in **Figure 20**, SHPiP exhibits worse and worse h/h_0 after each pool boiling test due to the above-mentioned hydrophilicity degradation. Comparing with SHPiP, SHPiM exhibits better h/h_0 than that of SHPiP every time. This is attributed to the fact that microchannel on the SHPiP can provide liquid replenishment to some extent, leading to the higher h/h_0. Also, after first pool boiling experiment, h/h_0 of SHiP exhibits a significant trend of decrease when the heat flux is higher than 20 W/cm^2 in the second and third experiment. According to the measurement of contact angle after pool boiling experiment in **Figure 20**, SHPiP and SHPiM transfer its hydrophilicity to hydrophobicity after 3rd pool boiling experiment. The contact angle of SHPiP and SHPiM is 142° and 136°, respectively. As aforementioned, vapor film formation resulting from increased bubble escape resistance weakens pool boiling performance.

Different from SHPiP and SHPiM, SHPiW-SHPoB and SHPoW-SHPiB exhibit an increased trend of h/h_0 range from 0 to 60 W/cm^2. This is attributed to the fact that above-mentioned heterogeneous wettability and microchannel corner can facilitate the bubble nucleation for enhancing nucleate boiling. After three repeated pool boiling experiments, the partial super-hydrophillic areas can transfer to the hydrophobic areas, while a few areas may maintain hydrophilicity. Therefore, SHPiW-SHPoB and SHPoW-SHPiB can also facilitate bubble generation at a low heat flux and promote liquid replenishment at a high heat flux on these areas with heterogeneous wettability, resulting a continuous growth of h/h_0 after three repeated experiments.

However, SHPoW-SHPiB exhibits worse pool boiling performance than that of SHPiW-SHPoB. As aforementioned, using the hydrophilic microchannel wall of SHPiW-SHPoB, liquid replenishment can be offered timely for rewetting dry-spot resulting from bubble departure. After 3rd pool boiling experiment, the contact angle of SHPiW is 125°, which also exhibits the hydrophilicity degradation phenomenon. Some partial areas of SHPiW-SHPoB's wall may also maintain hydrophilicity, and capillary liquid can flow through these hydrophilic areas for rewetting the remaining nucleation sites to enhance pool boiling performance. Comparing with SHPiW-SHPoB, super-hydrophobic wall of SHPoW-SHPiB can always act as nucleation sites for bubble generation. After three repeated pool boiling experiments, vapor film has covered SHPoW-SHPiB at a high heat flux, preventing bubble release and liquid replenishment. Therefore, h/h_0 has started to decrease at a high heat flux in the 3rd experiment. As shown in **Figure 21**, after three repeated experiments, partial vapor film can be formed on SHPiW-SHPoB at a high heat flux, while entire vapor film can be formed on SHPoW-SHPiB at a high heat flux. Liquid-vapor separation can still exist on SHPiW-SHPoB to promote liquid replenishment and facilitate bubble escape for continuously enhancing pool boiling performance. Comparing with SHPiW-SHPoB, faster formation of entire vapor film contributes to faster decrease of SHPoW-SHPiB's pool boiling performance.

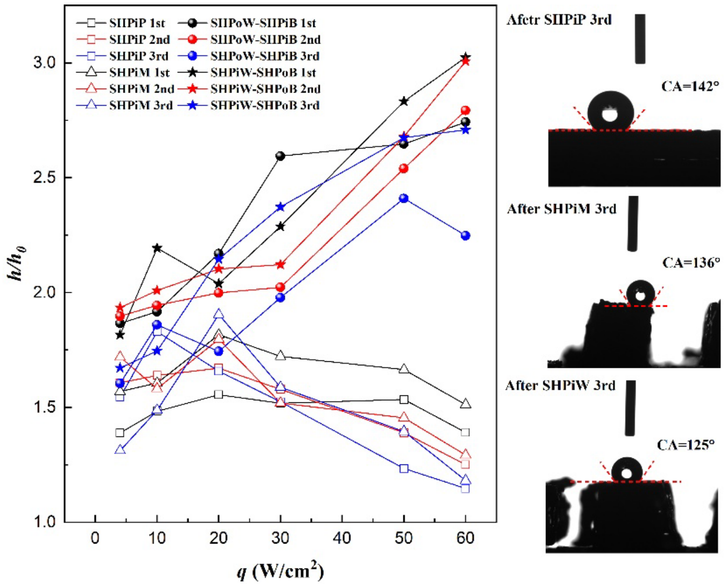

Figure 20. h/h_0 of SHPiP, SHPiM, SHPiW-SHPoB and SHPoW-SHPiB at different heat fluxes with three repeated experiments.

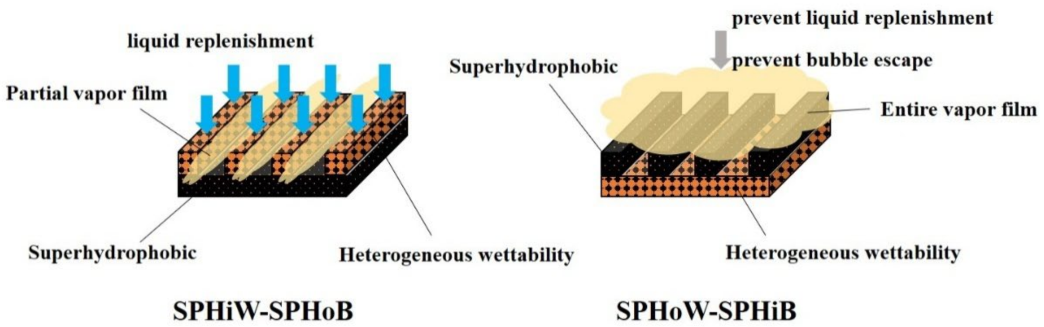

Figure 21. Boiling mechanism on SHPiW-SHPoB and SHPoW-SHPiB at a high heat flux after three repeated experiments.

4. Conclusions

Pool boiling heat transfer and bubble dynamics of copper foam with heterogeneous wetting vapor channels were systematically investigated. The following conclusions can be drawn:

(1) For the copper foam with uniform wettability, in the first pool boiling experiment, SHPoP can promote bubble nucleation, while SHPiP can improve capillary pumping and delay the maximum heat transfer coefficient at high heat flux. The average CHF of SHPoP is 72.1 W/cm^2 after three repeated experiments, hydrophilicity degradation can weaken pool boiling performance of SHPiP after three repeated experiments.

(2) For the copper foam microchannel with uniform wettability, UTM has an average CHF of 75.2 W/cm^2, which is 15% higher than that of UTP. The average CHF of

the SHPoM is 80.2 W/cm^2. The CHF of SHPiM decreases from 84 W/cm^2 to 74 W/cm^2 after three repeated experiments.

(3) For the copper foam microchannel with heterogeneous wettability, after three repeated experiments, the CHF of SHPoW-SHPiB decreases from 96.1 W/cm^2 to 82 W/cm^2, while the CHF of SHPiW-SHPoB decreases from 106.3 W/cm^2 to 90.4 W/cm^2.

(4) In the first, pool boiling heat transfer of SHPoW-SHPiB and SHPiW-SHPoB can be significantly enhanced by promoting bubble nucleation sites, facilitating bubble release, delaying bubble coalescence and separating vapor-liquid paths. SHPiW-SHPoB has the maximum h/h_0 of around 3, indicating that nucleate boiling can be maintained due to the vapor escape from super-hydrophobic foam microchannel and liquid supply from the super-hydrophilic foam wall.

(5) After three repeated pool boiling experiments, due to hydrophilicity degradation, liquid-vapor separation can still exist on SHPiW-SHPoB to promote liquid replenishment and facilitate bubble escape for continuously enhancing pool boiling performance. And faster formation of entire vapor film contributes to faster decrease of SHPoW-SHPiB's pool boiling performance.

Acknowledgements

This research is financially supported by National Key Research and Development Program (No.2022YFE0198800), and National Natural Science Foundation of China (No. 52076139).

References

[1] R. Wen, X. Ma, Y.-C. Lee, R. Yang, Liquid-Vapor Phase-Change Heat Transfer on Functionalized Nanowired Surfaces and Beyond, Joule, 2(11) (2018) 2307-2347.

[2] S.K. Singh, D. Sharma, Review of pool and flow boiling heat transfer enhancement through surface modification, International Journal of Heat and Mass Transfer, 181 (2021) 122020.

[3] J. Long, Z. Liu, H. Lin, Y. Li, Z. Cao, Z. Zhang, X. Xie, Pool boiling heat transfer and bubble dynamics over V-shaped microchannels and micropyramids: Does high aspect ratio always benefit boiling?, Applied Thermal Engineering, 201 (2022) 117796.

[4] G. Chen, M. Jia, S. Zhang, Y. Tang, Z. Wan, Pool boiling enhancement of novel interconnected microchannels with reentrant cavities for high-power electronics cooling, International Journal of Heat and Mass Transfer, 156 (2020).

[5] J. Li, G. Zhu, D. Kang, W. Fu, Y. Zhao, N. Miljkovic, Endoscopic Visualization of Contact Line Dynamics during Pool Boiling on Capillary-Activated Copper Microchannels, Advanced Functional Materials, 31(4) (2020) 2006249.

[6] S.H. Kim, G.C. Lee, J.Y. Kang, K. Moriyama, M.H. Kim, H.S. Park, Boiling heat transfer and critical heat flux evaluation of the pool boiling on micro structured surface, International Journal of

Heat and Mass Transfer, 91 (2015) 1140-1147.

[7] H.W. Moon, Y.J. Yoon, J.H. Park, B.-S. Myung, D.E. Kim, Dynamic wetting and boiling characteristics on micro-structured and micro/nano hierarchically structured surfaces, Experimental Thermal and Fluid Science, 74 (2016) 19-26.

[8] L. Duan, B. Liu, B. Qi, Y. Zhang, J. Wei, Pool boiling heat transfer on silicon chips with non-uniform micro-pillars, International Journal of Heat and Mass Transfer, 151 (2020) 119456.

[9] X. Kong, Y. Zhang, J. Wei, Experimental study of pool boiling heat transfer on novel bistructured surfaces based on micro-pin-finned structure, Experimental Thermal and Fluid Science, 91 (2018) 9-19.

[10] Z. Cao, B. Liu, C. Preger, Y.H. Zhang, Z. Wu, M.E. Messing, K. Deppert, J.J. Wei, B. Sunden, Nanoparticle-Assisted Pool Boiling Heat Transfer on Micro-Pin-Fin Surfaces, Langmuir, 37(3) (2021) 1089-1101.

[11] H. Tang, L. Xia, Y. Tang, C. Weng, Z. Hu, X. Wu, Y. Sun, Fabrication and pool boiling performance assessment of microgroove array surfaces with secondary micro-structures for high power applications, Renewable Energy, 187 (2022) 790-800.

[12] S. Jun, J. Kim, D. Son, H.Y. Kim, S.M. You, Enhancement of Pool Boiling Heat Transfer in Water Using Sintered Copper Microporous Coatings, Nuclear Engineering and Technology, 48(4) (2016) 932-940.

[13] W. Zhou, X. Hu, L. Mao, Y. He, Markedly enhanced pool boiling heat transfer performance on maicropaorous copper surfaces fabricated utilizing a facile wire cutting process, Applied Thermal Engineering, 165 (2020).

[14] S. Zhang, X. Jiang, Y. Li, G. Chen, Y. Sun, Y. Tang, C. Pan, Extraordinary boiling enhancement through micro-chimney effects in gradient porous micromeshes for high-power applications, Energy Conversion and Management, 209 (2020) 112665.

[15] D. Lee, B.S. Kim, H. Moon, N. Lee, S. Shin, H.H. Cho, Enhanced boiling heat transfer on nanowire-forested surfaces under subcooling conditions, International Journal of Heat and Mass Transfer, 120 (2018) 1020-1030.

[16] D. Lee, N. Lee, D.I. Shim, B.S. Kim, H.H. Cho, Enhancing thermal stability and uniformity in boiling heat transfer using micro-nano hybrid surfaces (MNHS), Applied Thermal Engineering, 130 (2018) 710-721.

[17] C.H. Choi, M. David, Z. Gao, A. Chang, M. Allen, H. Wang, C.H. Chang, Large-scale Generation of Patterned Bubble Arrays on Printed Bi-functional Boiling Surfaces, Sci Rep, 6 (2016) 23760.

[18] G.H. Seo, U. Jeong, H.H. Son, D. Shin, S.J. Kim, Effects of layer-by-layer assembled PEI/MWCNT surfaces on enhanced pool boiling critical heat flux, International Journal of Heat and Mass Transfer, 109 (2017) 564-576.

[19] S. Lee, G.H. Seo, S. Lee, U. Jeong, S.J. Lee, S.J. Kim, W. Choi, Layer-by-layer carbon nanotube coatings for enhanced pool boiling heat transfer on metal surfaces, Carbon, 107 (2016) 607-618.

[20] A. Akbari, E. Mohammadian, S.A. Alavi Fazel, M. Shanbedi, M. Bahreini, M. Heidari, G. Ahmadi, Comparison between Nucleate Pool Boiling Heat Transfer of Graphene Nanoplatelet- and Carbon Nanotube- Based Aqueous Nanofluids, ACS Omega, 4(21) (2019) 19183-19192.

[21] J. Xu, M. Yang, J. Xu, X. Ji, Vertically oriented TiO2 nanotube arrays with different anodization times for enhanced boiling heat transfer, Science China Technological Sciences, 55(8) (2012) 2184-2190.

[22] K. Lu, X. Wei, F. Xue, M. Liu, Semiconductor nanotubes enhance boiling heat transfer, International Journal of Heat and Mass Transfer, 164 (2021) 120597.

[23] G. Chen, C.H. Li, Combined effects of liquid wicking and hydrodynamic instability on pool boiling critical heat flux by two-tier copper structures of nanowires and microgrooves, International Journal of Heat and Mass Transfer, 129 (2019) 1222-1231.
[24] A.M. Gheitaghy, H. Saffari, M. Mohebbi, Investigation pool boiling heat transfer in U-shaped mesochannel with electrodeposited porous coating, Experimental Thermal and Fluid Science, 76 (2016) 87-97.
[25] J. Li, W. Fu, B. Zhang, G. Zhu, N. Miljkovic, Ultrascalable Three-Tier Hierarchical Nanoengineered Surfaces for Optimized Boiling, ACS Nano, 13(12) (2019) 14080-14093.
[26] J. Xu, X. Ji, W. Zhang, G. Liu, Pool boiling heat transfer of ultra-light copper foam with open cells, International Journal of Multiphase Flow, 34(11) (2008) 1008-1022.
[27] L.L. Manetti, A.S.O.H. Moita, R.R. de Souza, E.M. Cardoso, Effect of copper foam thickness on pool boiling heat transfer of HFE-7100, International Journal of Heat and Mass Transfer, 152 (2020) 119547.
[28] H. Hu, Y. Zhao, Z. Lai, C. Hu, Influence of surface wettability on pool boiling heat transfer on metal foam covers, International Journal of Thermal Sciences, 168 (2021) 107069.
[29] H. Hu, Y. Zhao, Z. Lai, C. Hu, Experimental investigation on nucleate pool boiling heat transfer characteristics on hydrophobic metal foam covers, Applied Thermal Engineering, 179 (2020) 115730.
[30] J. Shi, X. Jia, D. Feng, Z. Chen, C. Dang, Wettability effect on pool boiling heat transfer using a multiscale copper foam surface, International Journal of Heat and Mass Transfer, 146 (2020) 118726.
[31] A.M. Sharifzadeh, H. Moghadasi, H. Shakeri, H. Saffari, Influence of bubble departure control on nucleate pool boiling heat transfer of electrodeposited copper foam: Experiments and correlation, International Communications in Heat and Mass Transfer, 138 (2022) 106381.
[32] T. Li, X. Wu, Q. Ma, Pool boiling heat transfer of R141b on surfaces covered copper foam with circular-shaped channels, Experimental Thermal and Fluid Science, 105 (2019) 136-143.
[33] L. Zhou, W. Li, T. Ma, X. Du, Experimental study on boiling heat transfer of a self-rewetting fluid on copper foams with pore-density gradient structures, International Journal of Heat and Mass Transfer, 124 (2018) 210-219.
[34] C. Huang, H. Wang, E. Lichtfouse, Y. Tang, H. Xiang, Experimental study of multilayer gradient copper foam effect on pool boiling heat transfer performance and gas-liquid behavior characteristics, International Journal of Thermal Sciences, 183 (2023) 107856.
[35] A. Chaudhary, H.C. Barshilia, Nanometric Multiscale Rough CuO/Cu(OH)2 Superhydrophobic Surfaces Prepared by a Facile One-Step Solution-Immersion Process: Transition to Superhydrophilicity with Oxygen Plasma Treatment, The Journal of Physical Chemistry C, 115(37) (2011) 18213-18220.
[36] M.H. Alhosani, H. Li, A.S. Alketbi, Q. Guan, A. Aili, T. Zhang, Enhanced Liquid Propagation and Wicking Along Nanostructured Porous Surfaces, Advanced Engineering Materials, 23(7) (2021).
[37] A. Jaikumar, S.G. Kandlikar, Pool boiling inversion through bubble induced macroconvection, Applied Physics Letters, 110(9) (2017) 094107.
[38] A. Jaikumar, S.G. Kandlikar, Pool boiling enhancement through bubble induced convective liquid flow in feeder microchannels, Applied Physics Letters, 108(4) (2016) 041604.
[39] L.L. Manetti, G. Ribatski, R.R. de Souza, E.M. Cardoso, Pool boiling heat transfer of HFE-7100 on metal foams, Experimental Thermal and Fluid Science, 113 (2020).
[40] L. Mao, W. Zhou, X. Hu, Y. He, G. Zhang, L. Zhang, R. Fu, Pool boiling performance and bubble dynamics on graphene oxide nanocoating surface, International Journal of Thermal Sciences, 147 (2020).

[41] Q. Li, J. Zhao, X. Sun, B. Liu, Experimental investigation of pool boiling heat transfer on pillar-structured surfaces with different wettability patterns, Applied Thermal Engineering, 215 (2022) 118924.

[42] N. Zuber, On the Stability of Boiling Heat Transfer, Transactions of the American Society of Mechanical Engineers, 80(3) (2022) 711-714.

[43] A. Amiri, M. Shanbedi, H. Amiri, S.Z. Heris, S.N. Kazi, B.T. Chew, H. Eshghi, Pool boiling heat transfer of CNT/water nanofluids, Applied Thermal Engineering, 71(1) (2014) 450-459.

[44] W.M. Rohsenow, A Method of Correlating Heat-Transfer Data for Surface Boiling of Liquids, Transactions of the American Society of Mechanical Engineers, 74(6) (2022) 969-975.

[45] Z. Yao, Y.W. Lu, S.G. Kandlikar, Effects of nanowire height on pool boiling performance of water on silicon chips, International Journal of Thermal Sciences, 50(11) (2011) 2084-2090.

[46] H.S. Jo, T.G. Kim, J.-G. Lee, M.-W. Kim, H.G. Park, S.C. James, J. Choi, S.S. Yoon, Supersonically sprayed nanotextured surfaces with silver nanowires for enhanced pool boiling, International Journal of Heat and Mass Transfer, 123 (2018) 397-406.

[47] J. Han Kim, A. Gurung, M. Amaya, S. Muk Kwark, S.M. You, Microporous Coatings to Maximize Pool Boiling Heat Transfer of Saturated R-123 and Water, Journal of Heat Transfer, 137(8) (2015) 081501.

[48] M.-C. Lu, R. Chen, V. Srinivasan, V.P. Carey, A. Majumdar, Critical heat flux of pool boiling on Si nanowire array-coated surfaces, International Journal of Heat and Mass Transfer, 54(25-26) (2011) 5359-5367.

[49] D.I. Shim, G. Choi, N. Lee, T. Kim, B.S. Kim, H.H. Cho, Enhancement of Pool Boiling Heat Transfer Using Aligned Silicon Nanowire Arrays, ACS Appl Mater Interfaces, 9(20) (2017) 17595-17602.

[50] J. Long, J. Wu, Y. Zhou, X. Xie, Hydrophilicity degradation and steam-induced rewetting during capillary-fed boiling, Experimental Thermal and Fluid Science, 150 (2024).

[51] J. Long, M. Xi, P. Yang, Z. Huang, Mechanisms of metal wettability transition and fabrication of durable superwetting/superhydrophilic metal surfaces, Applied Surface Science, 654 (2024).

[52] H. Jo, D.I. Yu, H. Noh, H.S. Park, M.H. Kim, Boiling on spatially controlled heterogeneous surfaces: Wettability patterns on microstructures, Applied Physics Letters, 106(18) (2015) 181602.

[53] A. Jaikumar, S.G. Kandlikar, Enhanced pool boiling heat transfer mechanisms for selectively sintered open microchannels, International Journal of Heat and Mass Transfer, 88 (2015) 652-661.

[54] G. Chen, N. Chukwunenye, G.F. Jones, C.H. Li, Biomimetic Structures by Leaf Vein Growth Mechanism for Pool Boiling Heat Transfer Enhancements, International Journal of Heat and Mass Transfer, 155 (2020) 119699.

[55] A. Mehdikhani, H. Moghadasi, H. Saffari, An experimental investigation of pool boiling augmentation using four-step electrodeposited micro/nanostructured porous surface in distilled water, International Journal of Mechanical Sciences, 187 (2020) 105924.

[56] H. Yao, C. Zhou, Y. Li, H. Liu, Y. Wang, X. Wang, G. Li, Y. Zhu, Modification and pool boiling performance elevation of copper foam wicks for high power applications, Applied Thermal Engineering, 220 (2023).

[57] A.M. Sharifzadeh, H. Moghadasi, H. Saffari, M. Delpisheh, Experimental investigation of pool boiling heat transfer enhancement using electrodeposited open-cell metal foam, International Journal of Thermal Sciences, 176 (2022) 107536.

[58] Y.Y. Hsu, On the size of range of active nucleation cavities on a heating surface, Trans. ASME, 84

(1962).

[59] A. Walunj, A. Sathyabhama, Comparative study of pool boiling heat transfer from various microchannel geometries, Applied Thermal Engineering, 128 (2018) 672-683.

[60] B. Shen, M. Yamada, T. Mine, S. Hidaka, M. Kohno, K. Takahashi, Y. Takata, Depinning of bubble contact line on a biphilic surface in subatmospheric boiling: Revisiting the theories of bubble departure, International Journal of Heat and Mass Transfer, 126 (2018) 715-720.

[61] Y. Nam, J. Wu, G. Warrier, Y.S. Ju, Experimental and Numerical Study of Single Bubble Dynamics on a Hydrophobic Surface, Journal of Heat Transfer, 131(12) (2009).

[62] H. Jo, H.S. Ahn, S. Kang, M.H. Kim, A study of nucleate boiling heat transfer on hydrophilic, hydrophobic and heterogeneous wetting surfaces, International Journal of Heat and Mass Transfer, 54(25-26) (2011) 5643-5652.